

**THE DEVELOPMENT OF MICROSTRUCTURE IN
DUPLEX STAINLESS STEEL WELDS**

by
Naseem Issa Abdallah Haddad
Pembroke College
Cambridge

A dissertation submitted for the fulfilment
of the Degree of Doctor of Philosophy
at the University of Cambridge

December 1989

To
My Parents,
Rania, Ra'ad and Noor

PREFACE

This dissertation is submitted for the degree of Doctor of Philosophy at the University of Cambridge. The work described was carried out under the supervision and guidance of Dr. H.K.D.H. Bhadeshia at the Department of Materials Science and Metallurgy, Cambridge, between October 1986 and December 1989.

Except where acknowledgement and reference to previous work has been made, this work is, to the best of my knowledge, original and has not been submitted in whole or in part for a degree, diploma or other qualification at any other University.

I am grateful to the Royal Scientific Society of Jordan, the Chancellor of the University of Cambridge, the British Council, ESAB AB (Sweden) and Pembroke College for their financial support, and to Professor D. Hull for the provision of laboratory facilities at the University of Cambridge.

This dissertation contains less than sixty thousand words.

N.I.A Haddad

N. Haddad

15/12/1989

ACKNOWLEDGEMENTS

At the very beginning I would like to express my deepest gratitude to my supervisor Dr. H.K.D.H. Bhadeshia for his fruitful guidance and encouragement throughout the course of this project, and for his understanding and brotherly attitude. I consider myself fortunate to have had him as my supervisor.

I am grateful to his Royal Highness the Crown Prince of Jordan Al-Hasan Ben Talal for his interest in knowledge and his support for scientists. I am also grateful for my brother Ghaleb Haddad for his everlasting moral and financial support.

It is a pleasure to acknowledge the whole of the phase transformation group: Peter Wilson, Shahid Khan, Ashraf Ali, Manabu Takahashi, Roger Reed, Lihe Tan, Gethin Rees and Shafiq Mujahid for their encouragement and for the good times we spent together in Cambridge, and I wish Peter Wilson all the best in his work. Special thanks are due to Prof. Jer-Ren Yang for his help in my first year at Cambridge and to Dr. S. Atamert for the stimulating discussions and the transmission electron microscope sessions he spent with me. I would also like to thank Dr. Moazam Baloch for his friendship and to wish the new members of the group the best in their research. I should also acknowledge Dr. Alastair Sugden for his encouragement and advice.

Thanks are also extended to the technical staff of the department, in particular Mr. J. Leader for his help and technical advice on the dilatometer, Mr. D. Nichol (transmission electron microscopy) and Mr. Graham Morgan (workshop). I would also like to thank Mr. B. Barber and Mrs. C. Best for their help in preparing many slides, negatives and coloured prints for me and for their advice on photography. I should not also forget Mr. Ted Pettit for his help and cheerful face and Mrs. Katherine Stewart for her concern.

Finally, to my whole family and in particular: my mother for her prayers, my father for his endless support, my wife for her love and patience, my brothers; Rateb, Ghaleb, Salim, Jaser, Nasrallah for their encouragement and support, my sisters Laila, Rawda and Abba for their care and love and to my kids Ra'ad and Noor for being a reservoir of hope to me, for them all I would like to express my heartiest thanks and appreciation. Mr. Roger Reed should again be thanked for correcting this page.

The Development of Microstructure in Duplex Stainless Steel Welds

Abstract

Duplex stainless steels have a microstructure which is a mixture of δ -ferrite and austenite, and are used in fabrications requiring a good combination of corrosion resistance and strength. Both of these properties depend on the details of the microstructure, which is in turn a function of the exact chemical composition and thermomechanical history of the steel concerned. In order to avoid the large expense associated with the empirical development of such steels, and to be able to give guidance on the fabrication of welded joints, there is a need for a general model, based on phase transformation theory, which can estimate the microstructure.

The aim of the work presented in this thesis was to investigate the mechanisms for the development of microstructure in both wrought and welded duplex stainless steels with a view towards providing some of the fundamental data necessary for the prediction of microstructure. The thesis begins with an assessment of the literature on the physical metallurgy of duplex stainless steels. An experimental technique necessary to quantify the overall transformation kinetics of the δ -ferrite to austenite reaction is then presented. The technique is based on dilatometry and, after a variety of verification tests, was utilised in a comparative study of transformation kinetics in weld metal and wrought metal. It is demonstrated that because of the high oxygen concentration in the weld deposits, their transformation behaviour is rather insensitive to the parent δ -ferrite grain size, since the nonmetallic oxide particles serve as effective heterogeneous nucleation sites. The particles further serve to restrict the gross coarsening of the δ -ferrite grain size during elevated temperature heat-treatments. By contrast, the formation of austenite in wrought alloys containing much lower oxygen concentrations was found to be much more sensitive to the δ -ferrite grain size, which was in turn found to coarsen rapidly. These results are important in explaining the deficiencies in the volume fraction of austenite and properties reported for the microstructure in the heat affected zones of duplex stainless steel welds.

Further experiments are reported which elucidate the factors controlling the formation of allotriomorphic, Widmanstätten and "acicular" austenite. The experiments were carried out using detailed light and electron microscopy, microanalysis, surface relief studies *etc.*, and led, for example, to the discovery of conditions capable of suppressing the formation of undesirable Widmanstätten austenite to the benefit of acicular austenite and vice versa. The transformation has been studied under both isothermal and anisothermal conditions.

The effect of alloying additions has been examined using thermodynamic calculations, and the results have been verified experimentally.

CONTENTS

PREFACE	i
ACKNOWLEDGEMENTS	ii
ABSTRACT	iii
CONTENTS	iv
NOMENCLATURE & ABBREVIATIONS	ix
CHAPTER ONE	
<u>INTRODUCTION</u>	1
CHAPTER TWO	
<u>PHYSICAL METALLURGY OF DUPLEX STAINLESS STEELS</u>	
2.1 The elements in duplex stainless steel	7
2.1.1 <i>Iron</i>	7
2.1.2 <i>Chromium</i>	7
2.1.3 <i>Nickel</i>	9
2.2 Phase Equilibria in Binary Systems	9
2.2.1 <i>Cr-Fe</i>	9
2.2.2 <i>Cr-Ni</i>	12
2.2.3 <i>Fe-Ni</i>	12
2.3 Equilibria in Fe-Cr-Ni Systems	12
2.3.1 <i>Isothermal sections below the solidus temperature</i>	14
2.3.2 <i>Conclusion</i>	15
2.4 Effect of Alloying Elements on Duplex Stainless Steels	21
2.4.1 <i>Carbon and nitrogen</i>	21
2.4.2 <i>Molybdenum</i>	24
2.4.3 <i>Silicon</i>	24
2.4.4 <i>Niobium and titanium</i>	26
2.4.5 <i>Manganese</i>	26
2.4.6 <i>Copper</i>	26
2.4.7 <i>Platinum group metals Pd, Pt and Ru</i>	28

2.4.8 Chromium and nickel equivalents	28
2.5 δ to γ Isothermal and Continuous Cooling Transformation diagrams	31
2.5.1 Isothermal transformation diagrams	31
2.5.2 Discussion	34
2.5.3 Continuous cooling diagrams	35
2.6 Decomposition of δ in Duplex Stainless Steels	35
2.7 Sigma Phase Formation in Duplex Stainless Steels	38
2.8 Hydrogen in Duplex Stainless Steel	41
References	43

CHAPTER THREE

METALLURGY OF DUPLEX STAINLESS STEEL WELDS

3.1 Introduction	47
3.2 Solidification	47
3.2.1 Primary crystallisation of the weld pool	47
3.2.2 Microsegregation	48
3.2.3 Crystal growth during solidification	54
3.2.4 Primary crystallisation of stainless steel welds	54
3.2.5 Cooling rate	57
3.3 $\delta \rightarrow \gamma$ Transformation in Stainless Steel Weld Metals	58
3.4 Duplex Stainless Steel Weld Metals	59
3.4.1 Weld microstructure	59
3.4.2 Cooling rate	61
3.4.3 Effects of nitrogen and carbon on weld microstructure	61
3.4.4 Properties of weld metal and the heat affected zone	69
3.5 Precipitates in Duplex Stainless Steel Weld Metals	73
3.6 Empirical Estimation of the Microstructure of Duplex Welds	78
References	82

CHAPTER FOUR

EXPERIMENTAL TECHNIQUES

4.1 Introduction	86
4.2 Materials	86

4.3 Welding	86
4.4 Heat Treatment	88
4.5 Optical Microscopy	90
4.6 Dilatometry	90
4.6.1 Ni plating	92
4.7 X-ray Lattice Parameter Measurements	93
4.8 Hardness Measurement	95
4.8.1 Microhardness measurement	95
4.9 Surface Relief Experiments	95
4.10 Microanalysis	95
4.11 Transmission Electron Microscopy	96
4.12 “Seescan” Image Analysis	96
References	98

CHAPTER FIVE

EXPERIMENTAL STUDIES ON THE DEVELOPMENT OF MICROSTRUCTURE IN DUPLEX STAINLESS STEEL WELD METALS

5.1 Solidification	99
5.2 The Overall δ -Ferrite Content	113
5.3 Microanalysis	114
5.4 Microstructure of the Heat Affected Zone	117
5.5 Microstructure - Hardness Relationship	120
5.6 Inclusions	123
5.7 Conclusions	128
References	130

CHAPTER SIX

KINETICS AND METALLOGRAPHY OF THE δ – FERRITE TO AUSTENITE TRANSFORMATION IN DUPLEX STAINLESS STEEL WELD METALS

6.1 Transformation Behaviour of DSS Wrought and Weld Alloys	131
6.1.1 Isothermal dilatometry	131
6.1.2 The volume fraction of austenite	135
6.1.3 Lattice parameters and thermal expansion coefficients	136

Nomenclature

δ	δ -ferrite
γ	Austenite
Cr_{eq}	Chromium equivalent
Ni_{eq}	Nickel equivalent
α	Ferrite
T_{δ}	Ferritisation temperature
σ	Sigma phase
γ_w	Widmanstätten austenite
V_{γ}	Volume fraction of austenite

Abbreviations

b.c.c.	Body centred cubic
f.c.c.	Face centred cubic
CCT	Continuous-cooling-transformation
DSS	Duplex stainless steel
IPS	Invariant-plane strain
TTT	Time-temperature-transformation
HAZ	Heat affected zone
SCC	Stress corrosion cracking
MMA	Manual metal arc
TIG	Tungsten inert gas
EDS	Energy dispersive analysis
EELS	Electron energy loss spectroscopy
SA	Submerged arc
SEM	Scanning electron microscope
TEM	Transmission electron microscope
VHN	Vickers hardness number

Chapter 1

INTRODUCTION

During the last fifty years, duplex stainless steels have undergone considerable development, stimulated partly by the nickel shortages in the 1950's, late 1960's and 1970 [1]. They are now used extensively in the oil, gas, petro-chemical, paper and sugar industries [2]. Their unique combination of mechanical strength, thermal expansion coefficient [3], low temperature toughness and corrosion resistance, makes them suitable for a wide range of engineering applications: the high strength allows the design of lighter components and hence a reduction of costs in the piping so prominent in the oil industry. Their relatively low thermal expansivity when compared to austenitic stainless steels makes them useful for shell and tube heat exchangers, and the improved stress corrosion cracking resistance in chloride containing environments at temperatures above 50°C qualifies duplex stainless steels as alternatives for the classical austenitic stainless steel (Fe-18Cr-8Ni wt.%) which is dogged by stress corrosion problems [4]. Duplex stainless steels are characterised by a microstructure consisting of austenite (γ) grains in a δ -ferrite matrix or vice-versa [5]. The duplex microstructure is produced by the adjustment of the δ and γ stabilising alloying elements. The alloys are designed so that both phases contain sufficient chromium to render the steel as a whole "stainless" by producing a continuous and regenerating Cr_2O_3 film. Typical compositions and properties of industrial duplex stainless steels are listed in Tables 1.1 and 1.2.

The yield strength of duplex stainless steels increases with increasing δ -ferrite content and can reach twice that of austenitic stainless steel. A typical duplex stainless steel, Fe-26Cr-4Ni-2.5Mo-1.5Cu wt.%, has a minimum yield strength of 435 MPa at room temperature, while that of austenitic stainless steel (Fe-18Cr-8Ni-0.08C-2Mn-1Si wt.%) is only around 215 MPa. The ultimate tensile strength at room temperature rises to a maximum at about 70 to 80 vol% δ and then decreases as the alloy tends towards a fully ferritic structure [6]. A law of mixtures does not apply to the strength, probably because the austenite transforms during deformation and because it is unlikely that the deformation is homogeneously distributed between the phases.

Duplex stainless steels are superplastic at temperatures near 950°C, with elongation in tension of about 500%, if their grain size is sufficiently fine (3 to 10 μm) [7,8]. Even coarse grained duplex stainless steels can be super-plastic at temperatures above

1000°C and low strain rates, below 10^{-4} per second, the highest strain rate sensitivity being achieved when the volume fractions of ferrite and austenite are identical [9].

The corrosion resistance of duplex stainless steels is about the same as that of austenitic stainless steels for pitting and general corrosion, but as pointed out earlier, they possess an improved resistance to stress corrosion cracking, crevice corrosion [10], and to grain boundary corrosive attack induced by chromium depletion [5]. The time to rupture in a stress corrosion cracking test in 42% boiling MgCl_2 solution, under an initial stress of 232 N/mm^2 for Fe-26Cr-5.5Ni-1.5Mo-0.2N wt.% duplex stainless steel is about 500 hours, while it is 1.6 to 6 hours for austenitic stainless steel (Fe-0.08C-17Cr-12Ni-2Mn-1Si wt.%) under the same conditions [11].

The desirable properties of duplex stainless steels mentioned earlier are obtained when the microstructure consists of about an equal mixture of austenite and δ -ferrite. The microstructure depends on the alloy composition and thermo-mechanical treatment. Duplex stainless steels are used frequently in the as-welded condition. During welding, the ferrite-austenite balance is disturbed both in the weld metal and in the heat affected zone as a result of the range of temperatures encountered, from the ambient temperature to the fusion temperature and the variable cooling rate. This leads to a drop in the impact toughness and chloride stress corrosion cracking resistance of the weld metal and particularly of the heat affected zone where a fully ferritic structure may be obtained. The δ -ferrite content of duplex stainless steel weld metals is still estimated by the well-known Schaeffler [12] diagram, and with the help of some other modified approaches (see 3.6), all based on representing the effect of alloying elements empirically in terms of a chromium equivalent (Cr_{eq}) if they stabilise ferrite or as nickel equivalent (Ni_{eq}) if they are austenite stabilisers (see 2.4.8). The Schaeffler diagram does not take into account the effects of the cooling rate nor of the parent phase grain size on the $\delta \rightarrow \gamma$ solid-state transformation.

The prediction of weld metal microstructure and related properties should ideally be through a model based on rigorous phase transformation theory, and progress towards the development of foundations for such a model is the major ultimate aim of this work.

The work presented in this dissertation is an attempt to understand the transformation behaviour in duplex stainless steels as well as the microstructure of duplex

stainless steel weld metals and to lay a possible foundation for the prediction of microstructure and related properties. In chapter two, the physical metallurgy of duplex stainless steels in general is reviewed, and that of welding in duplex stainless steel is reviewed in chapter three. Special attention is paid to the δ -ferrite to austenite solid-state transformation as it is the most crucial aspect in duplex stainless steel weld metals. The details of the experimental techniques relevant to the present work are reported in chapter four. In chapter five the development of microstructure in multirun weld deposits is investigated, including aspects of solidification, solid-state transformation in the as-welded and reheated zones and the effects of segregation and inclusions.

The prediction of microstructure in duplex stainless steels is as yet empirical, partly because there are limited data on the isothermal and continuous cooling transformation of δ -ferrite to austenite in both wrought and welded duplex stainless steel. Time temperature-transformation and continuous-cooling-transformation diagrams (TTT & CCT), provide basic data for low-alloy steels and not widely available for the duplex stainless steels, making it difficult to assess the effect of the chemical composition and temperature on transformation behaviour. In chapter six the dilatometric approach for detecting phase transformation kinetics is used to measure and follow changes in the overall austenite volume fraction, and to characterize the kinetic behaviour in both wrought and welded duplex stainless steels. The effect of the δ -ferrite grain size on the transformation behaviour is also explored using dilatometry together with the influence of inclusions on transformation behaviour.

Although weld microstructure does not in general evolve under equilibrium conditions, a comparison between the theory and experimental data, can nevertheless be useful in rationalising general trends and in emphasising quantitatively the role of alloy chemistry; in chapter seven, thermodynamic calculations carried out assuming two phase equilibrium, are presented and compared with some experimental data. In chapter eight the δ -ferrite to austenite transformation is studied under continuous cooling conditions and the combined effect of δ -ferrite grain size, cooling rate and inclusions on the formation of the austenite is investigated. The main conclusions and suggestions for future work are presented in the final chapter.

Table 1.1: Typical compositions of industrial duplex stainless steels, wt.% [4].

Specification	designation	C*	Mn	P*	S*	Si	Ni	Cr	Mo	N	Others
ASTM A182 ASTM A240 ASTM A789 ASTM A790	UNS S31200	0.03	2.0*	0.045	0.03	1.0*	5.5-6.5	24-26	1.2-2	.14-.2	
ASTM A182 ASTM A240 ASTM A789 ASTM A790 ASTM A815	UNS S31803	0.03	2.0*	0.03	0.02	1.0*	4.5-6.5	21-23	2.5-3.5	.08-.2	
ASTM A240 ASTM A479	UNS S32550	0.04	1.5*	0.04	0.03	1.0*	4.5-6.5	24-27	2-4	.1-.25	1.5 - 2.5♣
ASTM A789 ASTM A790	UNS S32550	0.04	1.5*	0.04	0.03	1.0*	4.5-6.5	24-27	2.9-3.9	.1-.25	1.5 - 2.5♣
ASTM A240	UNS S32900	0.08	1.0*	0.04	0.03	0.75*	2.5-5.0	23-28	1-2	—	
ASTM A744	CD-4MCu	0.04	1.0*	0.04	0.04	1.0*	4.75- 6.0	23.5- 26.5	1.75- 2.25	—	2.75- 3.25♣
ASTM A789 ASTM A790	UNS S31500	0.03	1-1.2	0.03	0.03	1.4-2	4.3-5.3	18-19	2.5-3.0	—	
ASTM A89 ASTM A790	UNS S31250	0.03	2.0*	0.03	0.03	0.75*	5.5-7.5	24-26	2.5-3.5	.1-.3	.2 - .8♣ 0.1 - 0.5†
Wr no 1.4417	X2 CrNiMo Si 195	0.03	2.0*	0.045	0.03	1.5-2	4.5-5	18-20	2.5-3.5	—	
Wr no 1.4460	X8 CrNiMo 27 5	0.1	2.0*	0.045	0.03	1.0*	4.0-5	26-28	1.3-2.0	—	
Wr no 1.4462	X2 CrNiMo 22 5	0.03	2.0*	0.03	0.02	1.0*	4.5-6.5	21-23	2.5-3.5	.08-.2	
Wr no 1.4582	X4 CrNiMo Nb 25 7	0.06	2.0*	0.045	0.03	1.0*	6.5-7.5	24-26	1.3-2.0	—	♠

* Maximum, ♣ Cu concentration, † W concentration, ♠ Nb (min.) = 10 × %C.

Table 1.2: Typical mechanical and physical properties of duplex stainless steel [4].

Specification	Designation	UTS N/mm^2	YS N/mm^2	E min, %	R min, %	HB	TC $W/m^{\circ}C$	e ($^{\circ}C/^{\circ}C$) $(\times 10^{-6})$
ASTM A182	UNS S31200	690 [†]	450	25	50	—		
ASTM A240		690	450	25	—	220		
ASTM A789		690	450	25	—	280		
ASTM A790		690	450	25	—	280		
ASTM A182	UNS S31803	620	450	25	45	—	19-21	13.1-13.7
ASTM A240		620	450	25	—	290		
ASTM A789		620	450	25	—	290		
ASTM A790		620	450	25	—	290		
ASTM A815		620	450	25	—	290		
ASTM A240	UNS S32550	760	550	15	—	297		
ASTM A479								
ASTM A789	UNS S32550	760	550	15	—	297		
ASTM A790								
ASTM A240	UNS S32900	620	485	15	—	271		
ASTM A744	UNS CD-4MCu	690	485	16	—	—		
ASTM A789	UNS S31500	630	440	30	—	290	20	13.1
ASTM A790								
ASTM A789	UNS S31250	760	550	15	—	297		
ASTM A790								
Wr No 1.4460	X8 CrNiMo 275	640 [†]	490	25	—	230♣		
Wr No 1.4582	X4 CrNiMo Nb 257	640 [†]	490	25	—	230♣		

UTS is the minimum tensile strength. YS is the minimum yield strength. E is elongation measured on 50 mm. gauge length. R is the reduction in area. HB is maximum Brinell hardness. TC is the thermal conductivity at 20°C. e is the thermal expansion for the temperature range 20 - 200°C.

[†] Maximum tensile strength is 900 N/mm^2 . ♣ Minimum Brinell hardness is 190.

References

1. Roscoe, C. V. and Gradwell, K. J. Conf. Proc. 'Duplex Stainless steel', October 1986, The Hague, Publ. by Nederlands Instituut Voor Lastechniek, p. 126.
2. Craig, B. D. Conf. Proc. 'Duplex Stainless Steels', St. Louis, USA, 1982, Publ. by ASM, 1983, p. 293.
3. Elmer, J. W., Olson, D. L. and Matlock, D. K. (1982) Weld. J., Weld. Res. Suppl., p. 293s.
4. Street, J. (1986) Met. Const., p. 565.
5. Leslie, W. C. 'The Physical Metallurgy of Steels' (1981), McGraw-Hill Hemisphere Publ. Corp., Washington.
6. Hayden, H. W. and Floreen, S. (1973) Met. Trans., **4**, p. 561.
7. Hayden H. W. et al. (1967) Trans. Am. Soc. Met., **60**, p. 3.
8. Hayden H. W. et al. (1968) Trans. Am. Soc. Met., **61**, p. 85.
9. Adeniyi, A. Conf. Proc. 'Duplex Stainless Steels', St. Louis, USA, 1982, Publ. by ASM, 1983, p. 143.
10. Cunningham, E. R. (1972) Met. Prog., p. 57.
11. Truman, J. E. and Prit, K. R. Conf. Proc. 'Duplex Stainless Steels', St. Louis, USA, 1982, Publ. by ASM, 1983, p. 113.
12. Schaeffler, L. A. (1949) Metal Progress, **56**, p. 680.

Chapter 2

PHYSICAL METALLURGY OF DUPLEX STAINLESS STEELS

The physical metallurgy of duplex stainless steel is best approached initially via phase diagrams, which help rationalize the role of the alloying elements on phase transformations.

2.1 The Elements in Duplex Stainless Steel

2.1.1 Iron

Pure iron exists in two allotropic forms at temperatures below its melting point (1536°C) and at ambient pressure [1] Table (2.1). The Curie temperature of the body centred cubic form lies between 767 and 771°C [2]. The phase equilibria of binary and higher systems of iron depend roughly on whether the added elements are more soluble in b.c.c. or in f.c.c. iron. Solid solutions in the f.c.c. and b.c.c. phases are designated γ and α respectively [3].

Table 2.1: Allotropes of Iron at Ambient Pressure [1].

Temperature Range (°C)	Symbol	Crystal Structure
1536 - 1392	δ	body centred cubic (b.c.c.)
1392 - 911	γ	face centred cubic (f.c.c.)
911 and below	α	body centred cubic (b.c.c.)

Using a sequence of vertical sections through the ternary phase diagram of the Fe-Cr-Ni system at various Fe contents, Fig. 2.1, Pugh and Nisbet [4] showed the effect of Fe content on the shape of the α and γ phase fields. As the iron concentration increases, the $\alpha/(\alpha + \gamma)$ and $\gamma/(\alpha + \gamma)$ phase boundaries become curved restricting the δ and $(\delta + \gamma)$ phase fields at higher temperatures and broadening the α and $(\alpha + \gamma)$ phase fields at low temperatures. At 90 wt.% Fe, the δ phase is separated completely from α by the γ phase field.

2.1.2 Chromium

Duplex stainless steels can contain between 18 to 30 wt.% of chromium, which has a b.c.c. structure below its melting point of approximately 1900°C [1,3]. It is considered

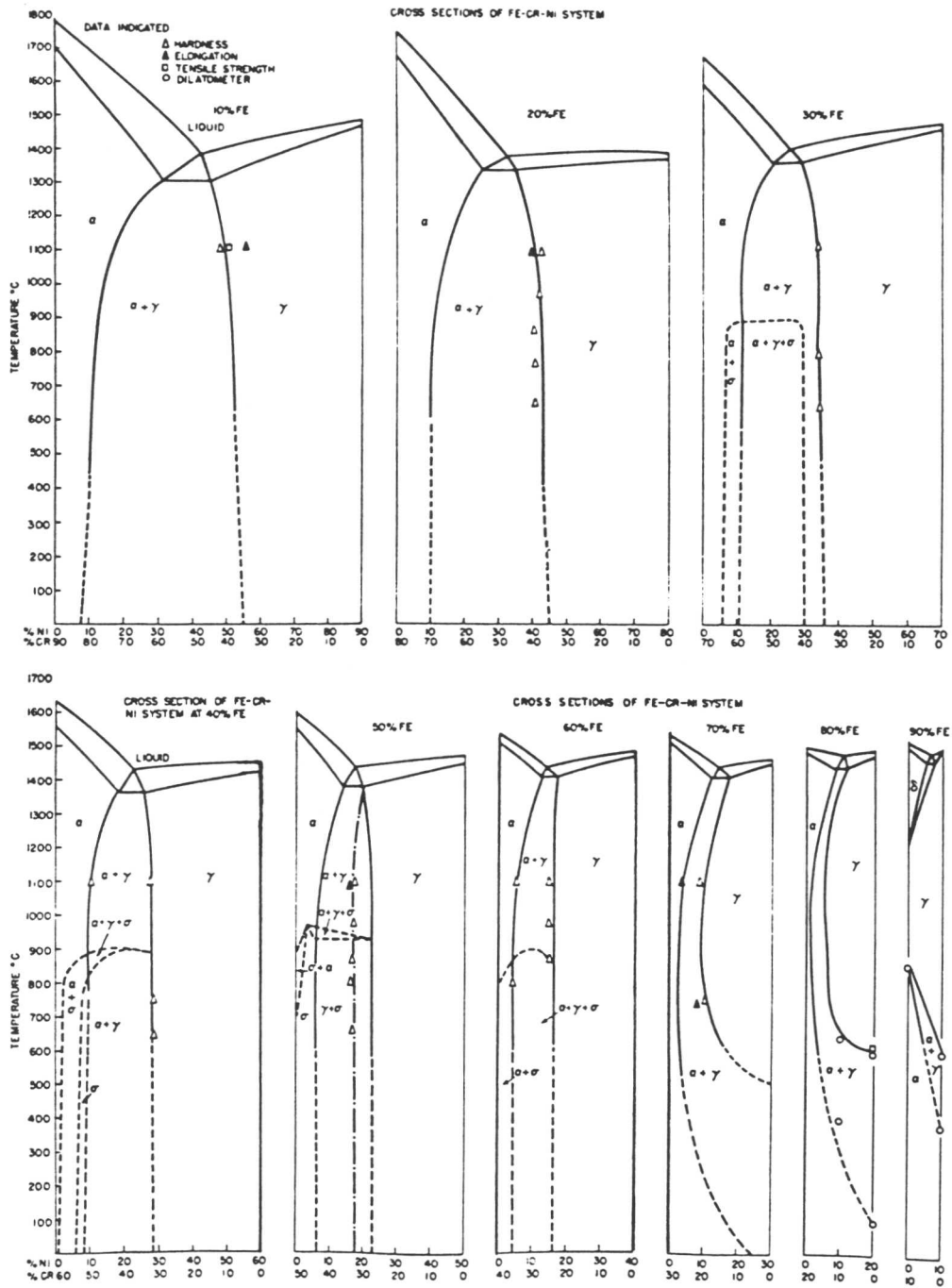


Fig. 2.1: Cross sections of the Fe-Cr-Ni system [4]. The concentrations are in weight percent.

to be the main ferrite stabiliser and is used to represent the effect of other alloying elements if they are also ferrite stabilisers, in the form of a “chromium equivalent” as in the Schaeffler diagram. The analysis in terms of ferrite or austenite stabilisers seems to be weak and not always representative of the element concerned over the entire temperature range of interest. At the same time that Cr apparently decreases the extent of the γ phase field, to a closed loop with a maximum solubility of about 12 wt.% Cr at about 1000°C [5], it also decreases the M_s temperature implying that it is a γ stabiliser:

$$M_s(^{\circ}\text{C}) = 502 - 810(C) - 1230(N) - 13(Mn) - 30(Ni) - 12(Cr) - 54(Cu) - 46(Mo) \quad [6]$$

where the alloying elements concentrations are in wt.%.

2.1.3 Nickel

Duplex stainless steels usually contain 5 to 9 wt.% Ni. Nickel is f.c.c. below its melting point of 1453°C and has a Curie temperature of between 352 and 360°C [1,2]. Its solubility in α -Fe reaches a maximum between 400 and 500°C. It stabilises γ so that the γ phase field extends at 30 wt.% Ni from about 500 to about 1450°C [5]. Ni has a strong effect on the M_s temperature, an increase of Ni content from 20 wt.% to 30 wt.% to 34 wt.% decreasing the M_s temperature from 200°C to 0°C to -220°C respectively [5]. It has often been used to represent the effect of other alloying elements which tend to stabilise austenite, with the help of an empirical “nickel equivalent”.

2.2 Phase Equilibria in Binary Systems

2.2.1 Cr-Fe

Chromium and b.c.c. iron form solid solutions in all proportions. The Cr-Fe binary phase diagram Fig. 2.2 [1,7,8-11] shows a simple liquidus and solidus which passes a minimum at 1510°C and around 18 wt.% Cr. The austenite field is a loop with a maximum solubility of 12 wt.% Cr, Fig. 2.3. The γ to α transformation temperature decreases as chromium is increased; it reaches a minimum at about 820°C and 8 wt.% Cr and then rises to join the δ -Fe to δ -Fe boundary and thus closes the γ loop [1,7]. The $\alpha + \gamma$ field is relatively narrow. The boundary positions of the $\alpha + \gamma$ field are very sensitive to interstitial solute content, Fig. 2.4. Slight additions of carbon or nitrogen increase the solubility of Cr in austenite and disproportionately expand the $\alpha + \gamma$ field. Alloys with

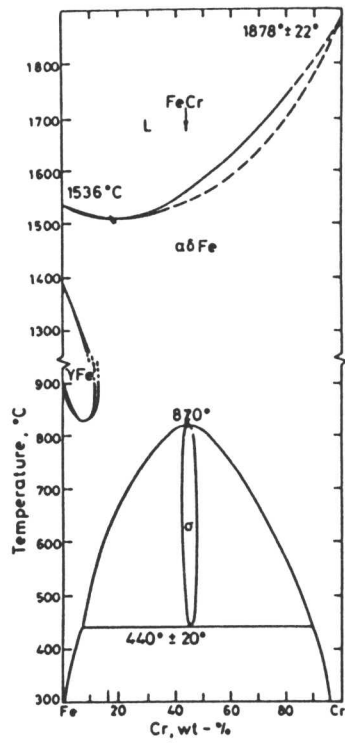


Fig. 2.2: Cr-Fe binary phase diagram [1,7-11].

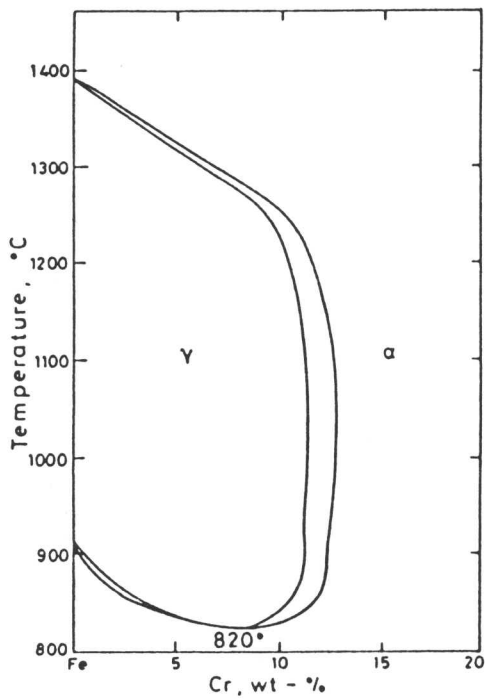


Fig. 2.3: γ loop of Cr-Fe binary phase diagram, interstitial content 50 ppm carbon and 900 ppm nitrogen [1,11].

more than about 12 wt.% chromium do not show any γ to α transformation, thus ruling out any means of grain refinement by phase transformation and the possibility of steel hardening by martensitic reaction. Other alloying additions are therefore made to extend the γ phase field of high chromium alloys.

Sigma phase appears at low temperatures $< 820^\circ\text{C}$, it forms very slowly from α in the temperature range between 800 and 600°C . Its composition range in the binary alloy is 46 to 53 wt.% Cr [5]. At temperatures below about 500°C a eutectoidal decomposition of σ to α and α' * take place. This reaction is also very sluggish which makes the phase boundary temperatures and compositions of σ a little uncertain.

2.2.2 Cr-Ni

The liquidus and solidus phase boundaries are well established for this system, Fig. 2.5, [2,7-9]. The eutectic composition is reliably placed at 49 wt.% Ni. The solubility of nickel is very restricted in α' at temperatures less than 1000°C , while in γ the solubility of chromium is less restricted to at least 20 wt.%, which when exceeded lead to the formation of CrNi_2 phase with an orthorhombic structure at around 580°C [1,7-9]. The transformation process in the Cr-Ni constitution diagram exerts no great influence on the properties of stainless steels, since their Ni and Cr contents are relatively low.

2.2.3 Fe-Ni

Nickel dissolves preferentially in γ -Fe so that austenite accounts for most of the phase diagram below the solidus, Fig. 2.6. The solubility of Ni in α -Fe and δ -Fe is restricted, it reaches a maximum in α -Fe between 400 and 500°C . At low temperatures below 450°C the detailed features of the Fe-Ni phase diagram are still in dispute. In the iron rich alloys the ordered face centred tetragonal phase FeNi can form at temperatures below 400°C implying that $\alpha + \text{FeNi}$ are the equilibrium phases [13]. At 345°C and 53 wt.% Ni γ decomposes eutectoidally to α and γ' (FeNi_3). The γ' crystal structure is primitive cubic and seems to have a wide range of stability, but at 503°C it transforms slowly to γ [9].

2.3 Equilibria in Fe-Cr-Ni Systems

Bain and Griffiths in 1927 [3] identified four phases in the Fe-Cr-Ni system, γ f.c.c. based on γ -Fe and Ni, α b.c.c. based on α -Fe, α' b.c.c. based on Cr and the σ

* α' is a chromium rich (62 - 83 wt.%) b.c.c. phase [76], which forms as a result of the miscibility gap in Fe-Cr binary system [77]. It can form by either nucleation and growth process (13 - 30 wt.% Cr) or by spinoidal decomposition (Cr $>$ 30 wt.%) [78].

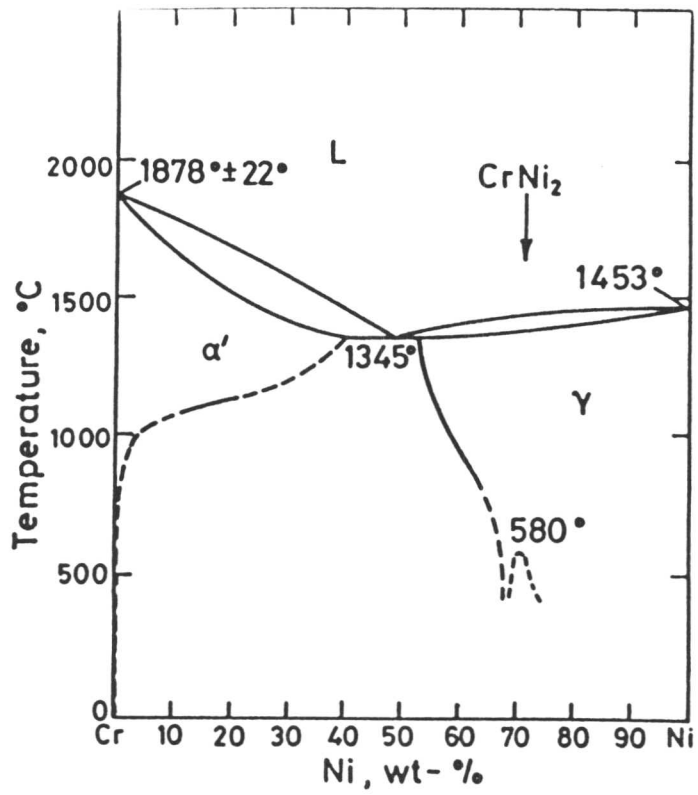


Fig. 2.5: Cr-Ni binary phase diagram [1,7-9].

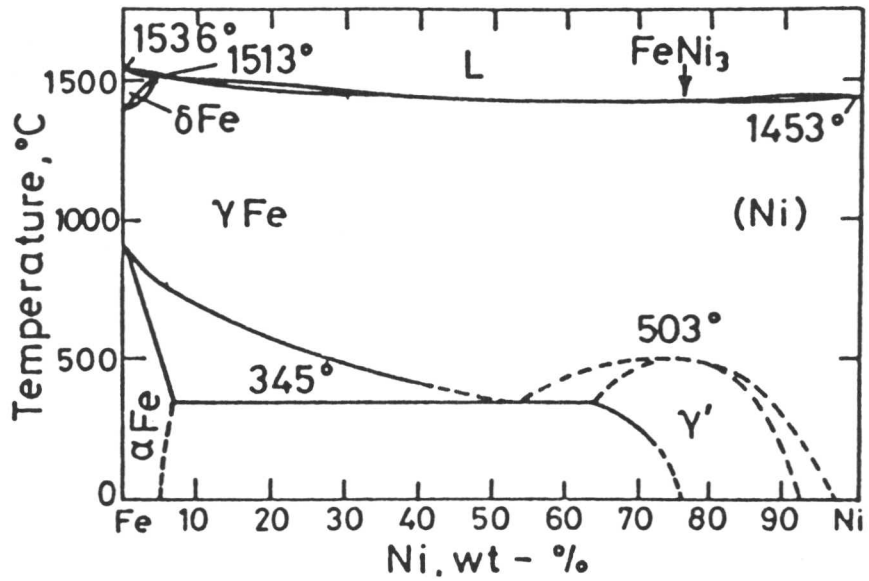


Fig. 2.6: Fe-Ni binary phase diagram [1,15].

phase.

The liquidus and solidus surfaces have been surveyed by a number of workers. Using dilatometric analysis the main regions from the Cr-Ni edge up to 95 wt.% Fe were confirmed by Wever and Jellinghaus in 1937 [16]. The purity of the alloys used was poor by today's standards, the silicon content being more than 1 wt.% in some cases. Nevertheless, in 1977, an investigation by Schurmann and Branckmann [15], confined to the iron rich corner of the phase diagram, in a region bounded by 21 wt.% Ni and 33 wt.% Cr, using modern techniques and pure materials, produced results which agreed fairly well with the earlier studies. However, in many cases no experimental data exist to define the phase boundaries precisely, so that regions of some of the ternary surfaces were defined by making them consistent with the accepted binary constitution at the edges of the diagrams, Fig 2.7; but some anomalies are known to remain [1].

2.3.1 Isothermal sections below the solidus temperature

Most publications agree on the number, the structure and the approximate composition limits at different temperatures of the solid phases present in the ternary Fe-Cr-Ni system mentioned earlier. The crucial factor is the influence of the σ upon equilibria in the solid state [1]. It is worth while noting that σ has a higher upper temperature limit in the ternary Fe-Cr-Ni systems than in the binary Fe-Cr system [17]. It may be located at 950 – 960°C on a vertical section through the ternary phase diagram at 50 wt.% Fe [18]. Isotherms that have been adapted from the more reliable papers are shown in Figs. 2.8, 2.9, 2.10, 2.11 [1]. Recent work has been carried out by Hoffmeister and Mundt [27], confined to the iron-rich part of the Fe-Cr-Ni ternary system for a region bounded by 23 to 38 wt.% Cr and 7 to 22 wt.% Ni. The $\delta - \gamma$ domain was found to widen with increasing Cr and Ni contents as well as decreasing annealing temperature, Figs. 2.12, 2.13, 2.14, 2.15.

Some of the duplex stainless steels investigated in the present work are plotted on the isothermal sections of the ternary Fe-Cr-Ni (Figs. 2.8 to 2.15), using the chromium and nickel equivalent values as calculated from some of the empirical formulae discussed later in more detail in section 2.4.8 after Schaeffler, DeLong and Noble *et al.* It is observed that variations in the empirical values of the equivalents, particularly nickel equivalent caused considerable scatter in the positions of the alloys on the phase diagram. The variation is mostly a result of the disagreement on the weights assigned for nickel and interstitials. Schaeffler used a factor of one for nickel, thirty for carbon and neglected the nitrogen. Noble *et al.* used a factor of two for nickel and twelve for both

carbon and nitrogen. Delong used a factor of one for nickel and gave more importance for interstitials by using a factor of thirty for both carbon and nitrogen. In comparison, the Schaeffler values push the positions towards the δ phase field while those according to Noble *et al.* push them towards the $\delta + \gamma$ phase field. The same positions according to Delong, lies inbetween. In general the positions on the isothermal sections using the chromium and nickel equivalent values are beneficial in enabling rough estimation of the microstructures and trends of the effects of alloying additions. The chromium and nickel equivalent empirical formulae used in literature are discussed in detail in (2.4.8).

2.3.2 Conclusion

There are some uncertainties in the knowledge of the relevant binary systems, uncertainties which are carried over into the Fe-Cr-Ni phase diagrams, and in the effect of other alloying additions such as C and N. These uncertainties do not seem to be of major importance and it should be possible to use the equilibrium phase diagram to set limits to aspects of the microstructure that is expected to be present in commercial alloys.

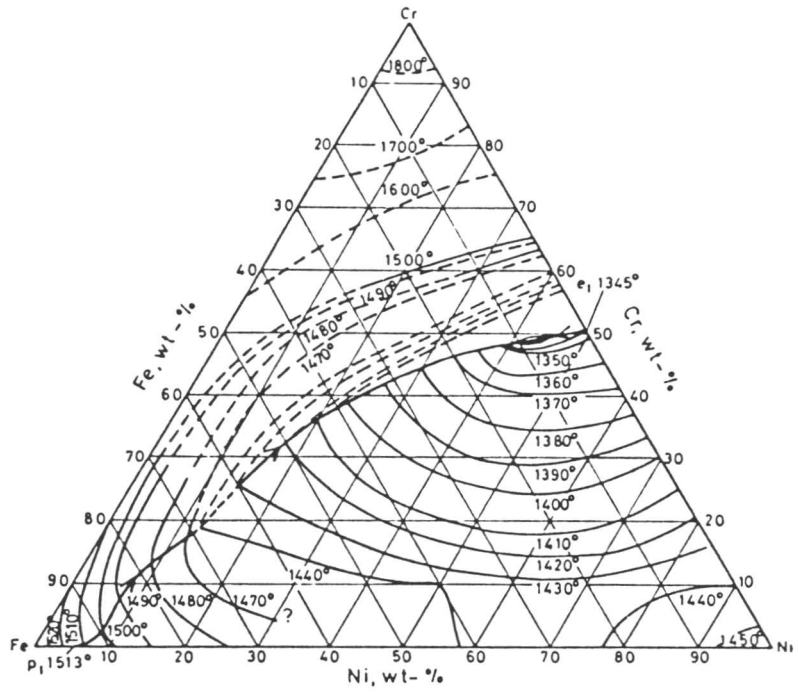


Fig. 2.7 a: Liquidus projection of Cr-Fe-Ni system [1,15].

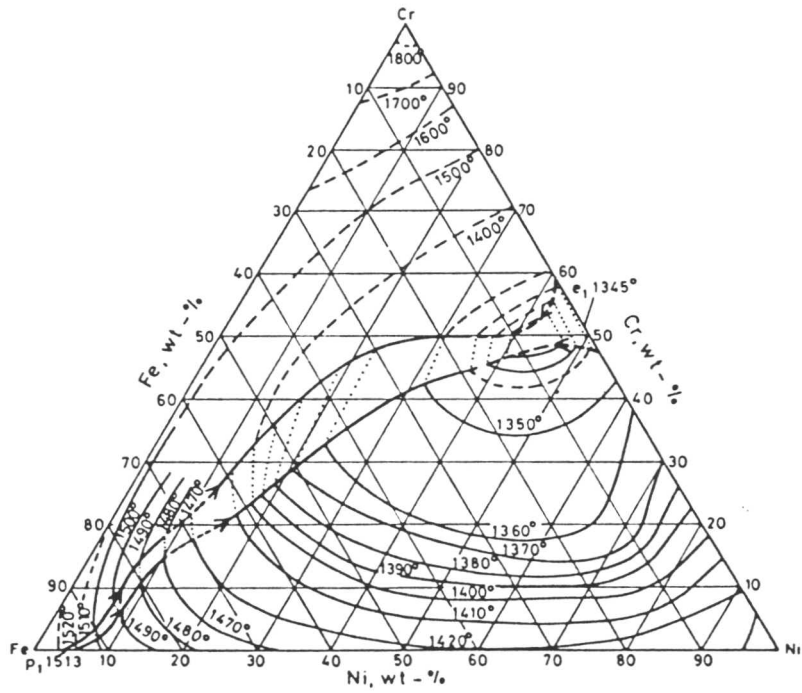


Fig. 2.7 b: Solidus projection of Fe-Cr-Ni system [1,15].

- SH, Delong
- + SH, Schaeffler
- △ SH, Noble
- SHP, Schaeffler

- ∅ WR4, Delong
- ▲ WR4, Noble
- WR4, Schaeffler

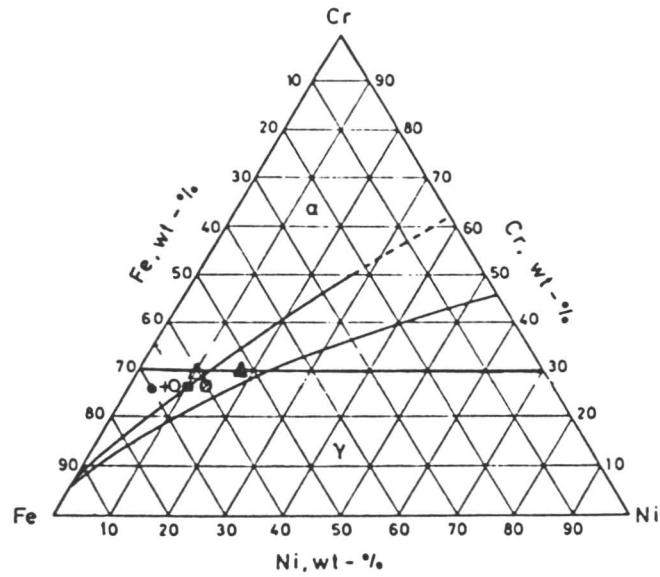


Fig. 2.8: 1300°C isotherm of Cr-Fe-Ni system [17].

- SH, Delong
- + SH, Schaeffler
- △ SH, Noble
- SHP, Schaeffler

- ∅ WR4, Delong
- ▲ WR4, Noble
- WR4, Schaeffler

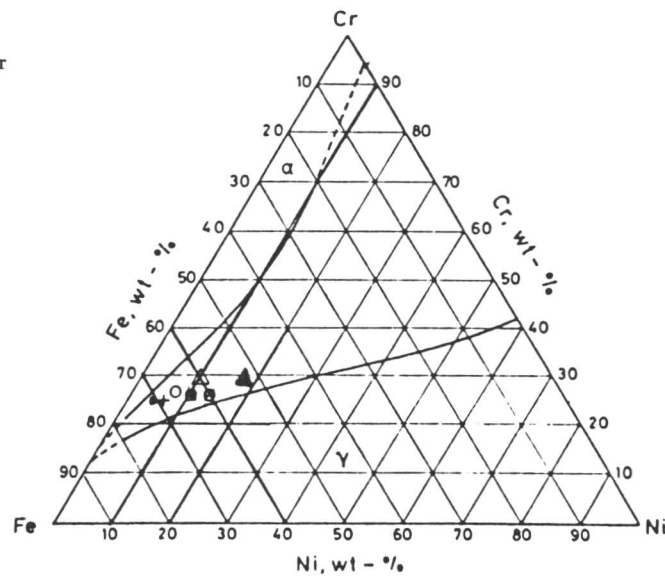


Fig. 2.9: 1000°C isotherm of Cr-Fe-Ni system [17].

- SH, Delong
- + SH, Schaeffler
- △ SH, Noble
- SHP, Schaeffler

- ⊘ WR4, Delong
- ▲ WR4, Noble
- WR4, Schaeffler

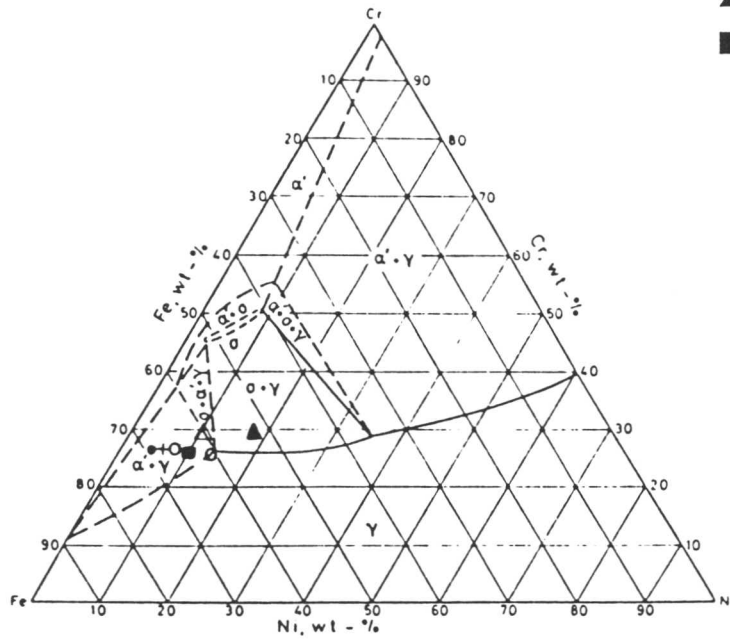


Fig. 2.10: 900°C isotherm of Cr-Fe-Ni system [17].

- SH, Delong
- + SH, Schaeffler
- △ SH, Noble
- SHP, Schaeffler

- ⊘ WR4, Delong
- ▲ WR4, Noble
- WR4, Schaeffler

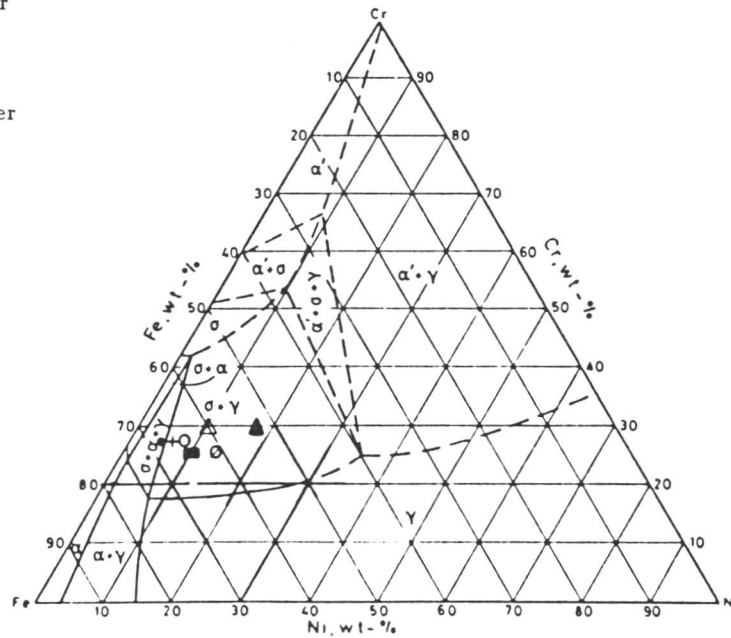


Fig. 2.11: 650°C isotherm of Cr-Fe-Ni system [17].

- SH, DeLong
- + SH, Schaeffler
- △ SH, Noble
- SHP, Schaeffler

- ⊙ WR4, DeLong
- ▲ WR4, Noble
- WR4, Schaeffler

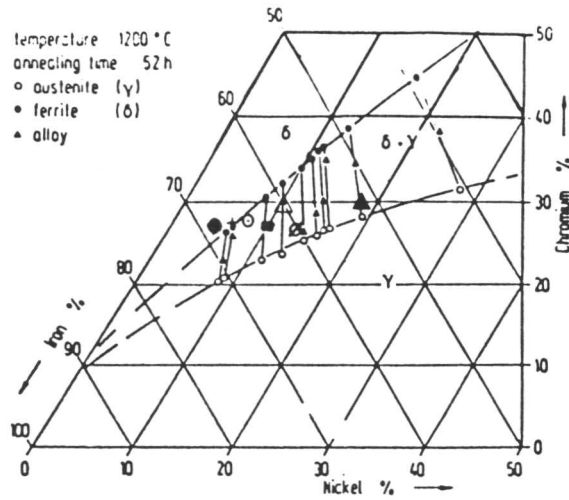


Fig. 2.12: Isothermal section at 1200°C of the Fe-Cr-Ni ternary diagram [19].

- SH, DeLong
- + SH, Schaeffler
- △ SH, Noble
- SHP, Schaeffler

- ⊙ WR4, DeLong
- ▲ WR4, Noble
- WR4, Schaeffler

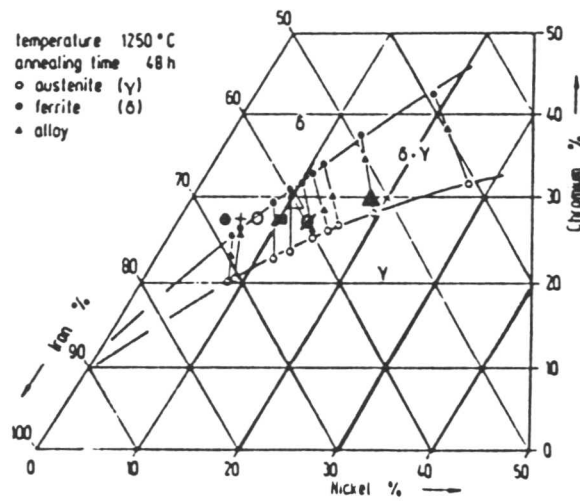


Fig. 2.13: Isothermal section at 1250°C of the Fe-Cr-Ni ternary diagram [19].

- SH, Delong
- + SH, Schaeffler
- △ SH, Noble
- SHP, Schaeffler

- ⊙ WR4, Delong
- ▲ WR4, Noble
- WR4, Schaeffler

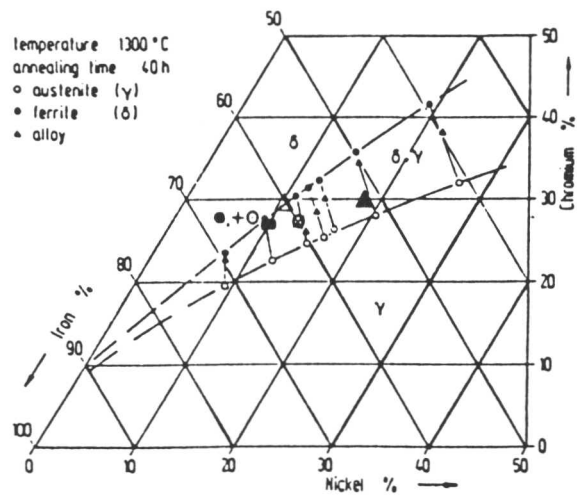


Fig. 2.14: Isothermal section at 1300°C of the Fe-Cr-Ni ternary diagram [19].

- SH, Delong
- + SH, Schaeffler
- △ SH, Noble
- SHP, Schaeffler

- ⊙ WR4, Delong
- ▲ WR4, Noble
- WR4, Schaeffler

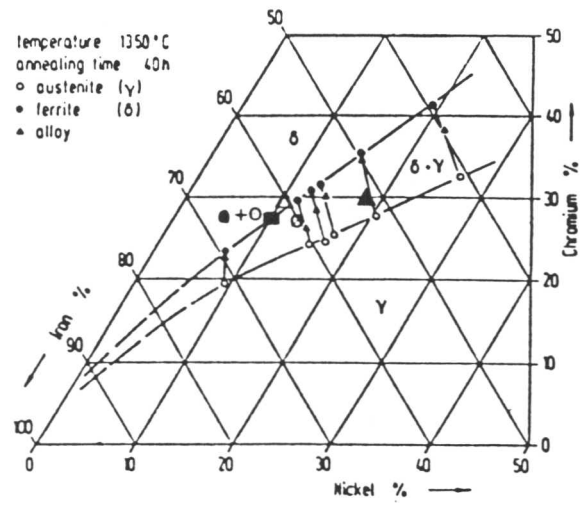


Fig. 2.15: Isothermal section at 1350°C of the Fe-Cr-Ni ternary diagram [19].

2.4 Effect of Alloying Elements on Duplex Stainless Steels

2.4.1 Carbon and nitrogen

Duplex stainless steels usually contain less than 0.08 wt.% carbon and up to 0.3 wt.% nitrogen. Both elements tend to stabilise austenite. The addition of C or N to Fe-Cr-Ni alloys expands the γ loop, thereby increasing the maximum solubility of Cr in austenite, a feature important for corrosion resistance. They also extend the $\alpha + \gamma$ field remarkably, Fig. (2.16). The solubility of carbon in austenitic stainless steels increases with temperature, Fig. (2.17) [20]. Precipitation of carbon as Cr_{23}C_6 at the austenite grain boundaries in austenitic stainless steels render them susceptible to intergranular corrosion by depleting chromium from solid solution [21]. In duplex stainless steels, carbon is found to be beneficial when precipitated as M_{23}C_6 , since this retards the formation of more detrimental intermetallic phases by tying up molybdenum [22].

Nitrogen is more soluble than carbon in the Fe-Cr-Ni system (Table 2.2). The addition of 3 to 5 wt.% Mn increases nitrogen solubility in (Fe-25Cr-7Ni-2Mo wt.%) duplex stainless steel castings to 0.35 wt.% with acceptable internal soundness. It is often used as a cheap nickel substitute in austenitic and duplex stainless steels [5].

Table 2.2: Temperature dependence of nitrogen solubility in types 304 and 308 stainless steels [23].

Temperature (°C)	Solid solubility of nitrogen in austenite (wt.%)	
	Type 304	Type 308
838	0.125	0.115
866	0.145	0.132
893	0.177	0.165
927	0.190	—
954	0.258	0.254
982	0.281	0.273
1010	—	0.297

The influence of increasing carbon and nitrogen contents to 0.13 wt.% and 0.27 wt.% respectively in Fe-24.5Cr-7Ni wt.% duplex stainless alloys on the $\delta \rightarrow \gamma$

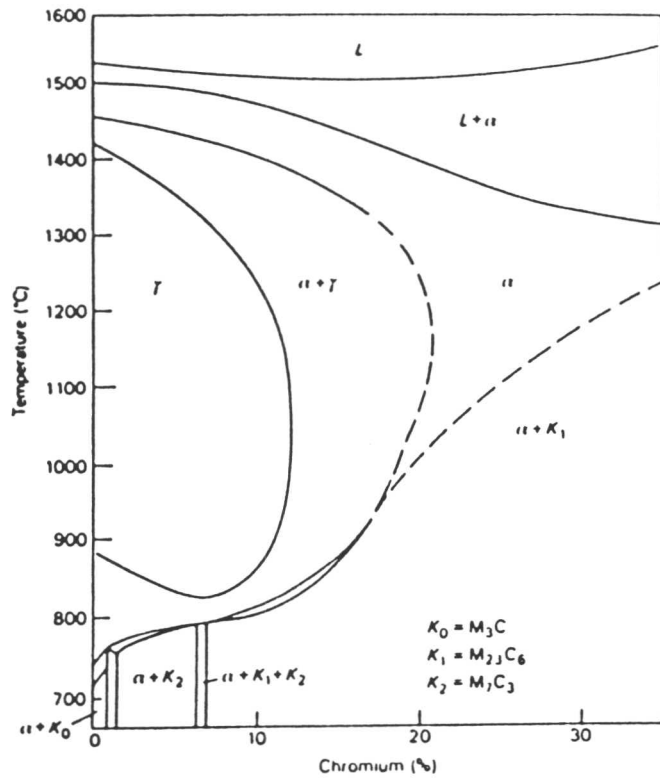


Fig. 2.16 a: Fe-Cr diagram at 0.05 wt.% C [24].

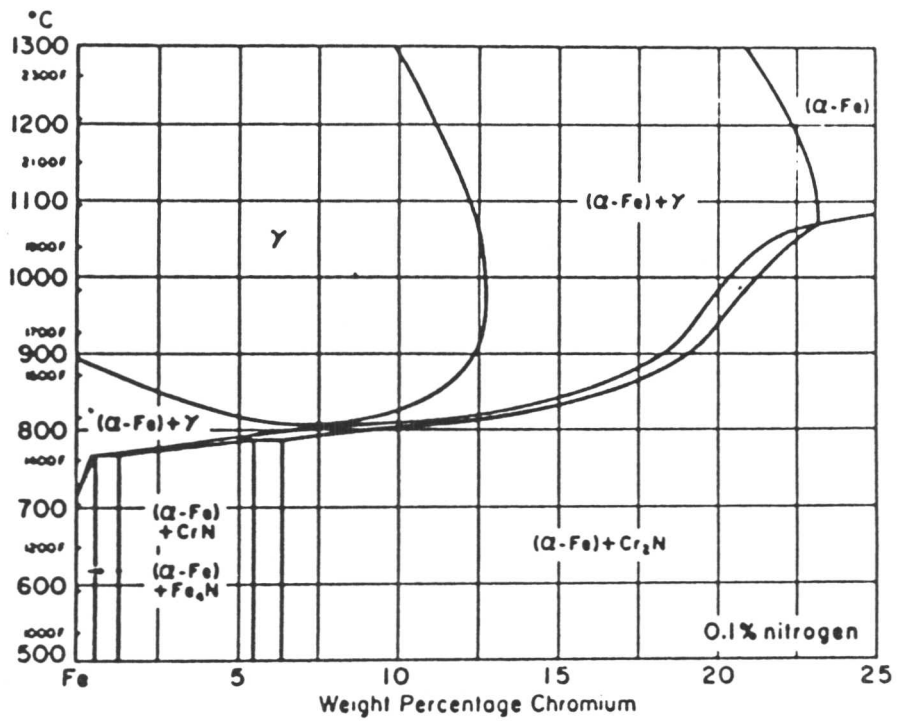


Fig. 2.16 b: Fe-Cr diagram at 0.1 wt.% N [25].

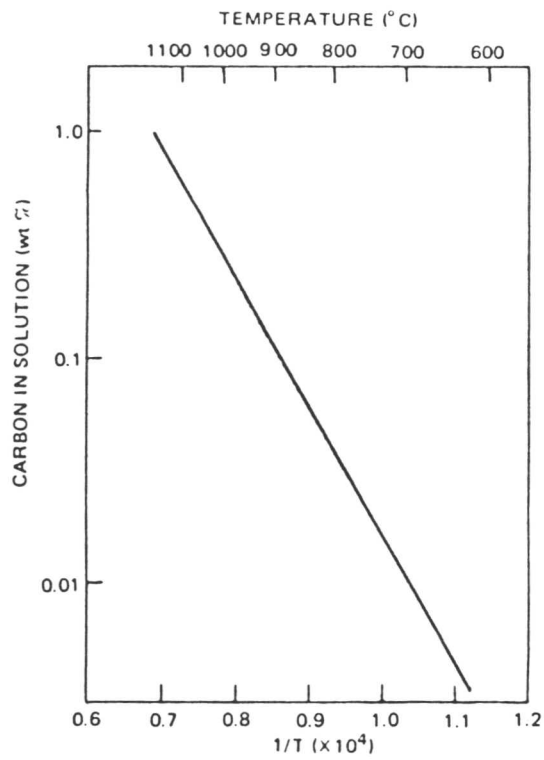


Fig. 2.17: Approximate solubility of carbon in 18wt.%Cr, 8-10 wt.%Ni, Fe alloys [20].

transformation was investigated by Hoffmeister and Mundt [26]. An increase in the C or N content causes a corresponding increase in the ferritisation temperature (T_δ) and retards the ferritisation process and subsequent grain growth during heat treatments above T_δ , Fig. 2.18. On cooling from the single δ phase region both elements lead to accelerated transformation and a reduction in the volume fraction of δ at room temperature.

2.4.2 Molybdenum

Duplex stainless steels usually contain 1 to 3.9 wt.% Mo. It is the third important alloying element in duplex stainless steel. It enhances the formation of ferrite [27], promotes the formation of σ phase and its most important effect is to improve the pitting corrosion resistance of duplex stainless steels. Molybdenum has a tendency to combine with iron to form intermetallic phases. The most important intermetallic compound it forms is the Laves (η) phase Fe_2Mo containing ≈ 45 wt.% Mo which can precipitate at a relatively low average molybdenum concentration of around 5 wt.% in the Fe-Mo binary alloys [28].

Intermetallic compound formation in the quaternary iron-chromium-molybdenum-nickel system has been investigated by Bechtold and Vacher [29]. They found that Laves and Chi phases could be induced to form at temperatures as high as 1093°C at an iron content of 70 wt.%, Fig. 2.19. At lower temperatures, an increase in molybdenum concentration was found to shift the tendency for sigma phase formation to alloys containing lower chromium and higher nickel concentrations.

2.4.3 Silicon

Silicon is a ferrite stabiliser; its effect is thought to be similar to molybdenum in expanding the δ -ferrite and ($\delta + \gamma$) range to the detriment of austenite in the Fe-Si binary system [30]. The addition of 3-5 wt.% Si to duplex stainless steel castings considerably improves the pitting resistance in acidified ferric chloride solution, and at the same time impairs the resistance to intergranular corrosion in boiling nitric acid solution [31]. It was believed that silicon forms a protective oxide layer when immersed in boiling nitric acid (a strong oxidising reagent), since this was the case with high silicon alloy exposed to air at elevated temperatures. The mechanism by which silicon increases the pitting resistance is not yet understood.

In heat resisting chromium and chromium-nickel steels, silicon additions of 1-3 wt.% are used to improve the scaling resistance [30]. In the Fe-Cr binary system

(Fig. 2.20), silicon expands the sigma phase range to lower chromium and higher temperatures [33,34]. It is also thought to have a similar effect on the ternary Fe-Cr-Ni system [30].

Silicon is believed to speed up the precipitation of $M_{23}C_6$ carbide in austenitic stainless steel, as it increases the activity of carbon [35]. In nitrogen containing stainless steels, silicon causes the precipitation of $M_{11}(CN)_2$ and thus slows down the precipitation of $M_{23}C_6$ carbide and sigma phase [36].

2.4.4 Niobium and titanium

Nb and Ti are ferrite formers. They also remove from solution the austenite stabilisers C and N to form NbC/NbN or TiC/TiN [37]. The addition of Ti to duplex stainless steel suppresses the formation of $M_{23}C_6$ as TiC precipitation is very rapid, and all the free carbon is consumed. Precipitation of TiC occurs only within the ferrite as insufficient Ti can dissolve in the austenite before the TiC precipitation is complete. Rapid removal of carbon from solution by titanium increases the Cr left in solution and hence can increase the rate of sigma formation [38].

2.4.5 Manganese

As mentioned earlier the analysis of the alloying element effects as α or γ stabiliser often proves to be inadequate. While Mn is considered an austenite stabiliser, additions of up to 8 wt.% Mn to duplex stainless steel castings, (Fe-25Cr-5Ni-2Mo wt.%) are found to have a small effect on the final volume fraction of austenite. On the other hand it promotes σ formation and increases the solubility of nitrogen [39]. Mn is important in duplex stainless steel weld metals as an oxygen and sulphur scavenger [40].

2.4.6 Copper

Copper is added to stainless steels in concentrations up to 3.5 wt.% to improve corrosion resistance and to increase tensile strength by means of precipitation hardening, which takes place as a result of the decreasing solubility of copper in ferrite as the temperature falls [34]. Ni and Cu are completely soluble in each other both in the liquid and solid states, while on the other hand, the solubility of copper in chromium is negligible. In the ternary Fe-Cr-Ni system, copper shows an austenitising effect which is weaker than that of nickel [41]. Copper-alloyed duplex stainless steels usually contain about 2 wt.% copper. Copper precipitation in duplex stainless steels is believed to produce

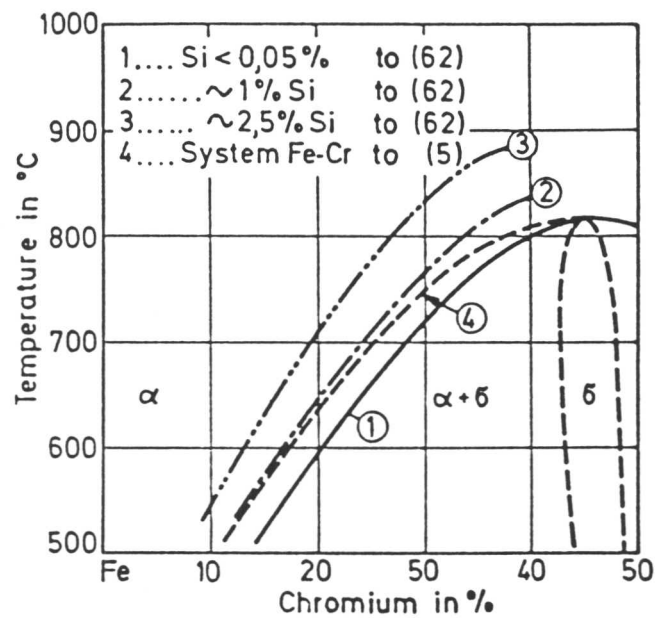


Fig. 2.20: Influence of silicon on the sigma phase range in the iron-chromium system [30]. (1-3) denote the influence of silicon, Schuller [33], (4) denotes the equilibrium phase boundaries, Kubaschewski [34].

austenite with very fine morphology by providing more copper/matrix interfaces to act as nucleation sites on the one hand, and on the other hand by pinning the growing austenite particles. The austenite particles were observed to inherit the twinned morphology of the copper particles on which they nucleated [42].

2.4.7 Platinum group metals Pd, Pt and Ru

Additions of up to 8 wt.% Pd, Pt and Ru to duplex stainless steels of base compositions (Fe-21Cr-6Ni wt.%) and (Fe-18Cr-6Ni wt.%), promotes an austenitic mode of solidification, reduces martensite formation in the solution treated and deformed materials and accelerates the formation of σ at 900°C on ageing [43].

2.4.8 Chromium and nickel equivalents

The effect of alloying elements in stainless steels has often been expressed in terms of “Ni equivalents” if they tend to stabilise austenite and as “Cr equivalents” if they stabilise ferrite. The different empirical formulae reported in the literature are listed below with the concentrations expressed in (wt.%):

$$\text{Cr}_{\text{eq}} = \text{Cr} + \text{Mo} + 1.5\text{Si} + 0.5\text{Nb}$$

$$\text{Ni}_{\text{eq}} = \text{Ni} + 30\text{C} + 0.5\text{Mn} \quad [44]$$

$$\text{Cr}_{\text{eq}} = \text{Cr} + \text{Mo} + 1.5\text{Si} + 0.5\text{Nb}$$

$$\text{Ni}_{\text{eq}} = \text{Ni} + 30\text{C} + 30\text{N} + 0.5\text{Mn} \quad [45]$$

$$\text{Cr}_{\text{eq}} = \text{Cr} + 2\text{Si} + 1.5\text{Mo} + 5\text{V} + 5.5\text{Al} + 0.75\text{Nb} + 1.5\text{Ti} + 0.75\text{W}$$

$$\text{Ni}_{\text{eq}} = \text{Ni} + \text{Co} + 0.5\text{Mn} + 0.3\text{Cu} + 30\text{C} + 25\text{N} \quad [27]$$

$$\text{Cr}_{\text{eq}} = \text{Cr} + 3\text{Si} + \text{Mo} + 10\text{Ti} + 4\text{Nb}$$

$$\text{Ni}_{\text{eq}} = \text{Ni} + 0.5\text{Mn} + 21\text{C} + 11.5\text{N} \quad [27]$$

$$\text{Cr}_{\text{eq}} = \text{Cr} + 3\text{Si} + 7\text{Ti} + 12\text{Al}$$

$$\text{Ni}_{\text{eq}} = \text{Ni} + 30\text{C} + 26\text{N} + 0.7\text{Mn} \quad [46]$$

$$\text{Cr}_{\text{eq}} = \text{Cr} + \text{Mo} + 3\text{Si}$$

$$\text{Ni}_{\text{eq}} = \text{Ni} + 15\text{C} + 10\text{N} + 0.7\text{Mn} \quad [47]$$

$$\text{Cr}_{\text{eq}} = \text{Cr} + 1.37\text{Mo} + 1.5\text{Si} + 2\text{Nb} + 3\text{Ti}$$

$$\text{Ni}_{\text{eq}} = \text{Ni} + 0.31\text{Mn} + 22\text{C} + 14.2\text{N} + \text{Cu} \quad [49]$$

$$\begin{aligned} \text{Cr}_{\text{eq}} &= \text{Cr} + 1.5\text{Mo} + 2\text{Mn} + 0.25\text{Si} \\ \text{Ni}_{\text{eq}} &= 2\text{Ni} + 12\text{C} + 12\text{N} \end{aligned} \quad [50]$$

$$\begin{aligned} \text{Cr}_{\text{eq}} &= \text{Cr} + \text{Mo} + 1.5\text{Si} + 0.5\text{Nb} \\ \text{Ni}_{\text{eq}} &= \text{Ni} + 30(\text{C} + \text{N}) + 0.5\text{Mn} \end{aligned} \quad [51]$$

As mentioned earlier, this method does not accurately represent the effect of the alloying elements because the elements can sometimes be both ferrite or austenite stabilising at the same time when considering different transformations, *e.g.* the effect of Cr in restricting the austenite phase field to a γ loop, and at the same time, depressing the M_s temperature. It is noticeable that the mentioned empirical formulae vary significantly and were in each case designed to solve specific problems and hence cannot be accepted as general solutions.

Chromium and nickel equivalents for the wrought and welded alloys investigated in this project as calculated using the above listed empirical formulae are shown in Table 2.3. The results show a larger variation in the nickel equivalent values compared with those of chromium equivalent. This is mainly a consequence of the variant weighting factors assigned in the empirical formulae for the interstitial elements carbon and nitrogen (both strong austenite formers). The role of nickel itself is differently represented, it has been given a weighting factor of one in the majority of the formulae, a recent formula [50] suggests it has a bigger effect. This formula further diminishes the effect of the interstitials by decreasing their weighting factor from the value of thirty suggested by Delong [45] to a figure of twelve. These discrepancies make it rather difficult to derive a general empirical formula and suggest that there is a need for a further investigation on the role of alloy chemistry in determining the microstructure, though the existing formulae are still useful in providing rough guidance for specific application.

Table 2.3: Chromium and nickel equivalent values of the alloys investigated in this project, as calculated from published empirical formulae.

Alloy		Reference								
		[44]	[45]	[27]	[27]	[46]	[47]	[49]	[50]	[51]
SH	Cr _{eq}	27.59	27.59	28.67	28.29	27.21	28.28	28.11	29.38	27.59
	Ni _{eq}	6.12	7.92	7.64	6.54	7.84	6.43	6.66	10.72	7.92
SHP	Cr _{eq}	27.95	27.95	29.10	27.96	25.66	27.96	28.80	29.10	27.95
	Ni _{eq}	4.95	5.43	5.35	5.04	5.36	4.96	5.09	9.59	5.43
W111	Cr _{eq}	30.08	30.08	32.23	32.77	31.17	32.51	30.77	30.68	30.08
	Ni _{eq}	7.94	10.6	10.18	8.3	10.44	7.9	8.5	12.48	10.61
WR2	Cr _{eq}	26.28	26.28	28.20	26.96	24.35	26.92	27.35	30.21	26.28
	Ni _{eq}	9.16	13.6	12.89	10.68	13.31	10.64	10.87	17.62	13.6
R2P	Cr _{eq}	27.43	27.43	29.35	27.95	24.45	27.95	28.72	31.38	27.43
	Ni _{eq}	8.76	8.76	8.76	8.58	9.02	8.72	8.35	15.25	8.76
R2PP	Cr _{eq}	26.5	26.5	27.92	26.51	23.68	26.51	27.54	27.92	26.5
	Ni _{eq}	9.3	9.73	9.66	9.41	9.67	9.35	9.45	18.47	9.73
WR4	Cr _{eq}	26.8	26.8	29.13	27.58	24.89	27.52	27.93	29.91	26.8
	Ni _{eq}	9.95	13.43	12.85	11.1	13.18	11.03	11.23	18.76	13.43
R4P	Cr _{eq}	26.42	26.42	28.12	27.03	24.03	27.03	27.53	30.02	26.42
	Ni _{eq}	8.36	8.36	8.36	8.18	8.62	8.32	7.95	14.22	8.36
SP1	Cr _{eq}	25.55	25.55	27.46	26.27	23.87	26.21	26.57	28.97	25.55
	Ni _{eq}	6.75	9.81	9.37	7.71	9.66	7.68	8.00	12.27	9.81
M22	Cr _{eq}	26.16	26.16	28.26	26.95	24.32	26.89	27.26	30.28	26.16
	Ni _{eq}	9.35	13.79	13.07	10.86	13.55	10.84	11.03	17.82	13.79
BW	Cr _{eq}	27.36	27.36	29.85	29.04	25.91	28.86	28.58	29.29	27.35
	Ni _{eq}	9.94	12.57	12.15	10.71	12.38	10.59	10.89	18.86	12.56
MELT3	Cr _{eq}	24.33	24.33	24.91	24.34	23.18	24.34	24.75	24.91	24.33
	Ni _{eq}	4.24	4.36	4.34	4.24	4.34	4.2	4.25	8.26	4.36
MELT4	Cr _{eq}	18.37	18.37	18.38	18.38	18.37	18.38	18.37	18.38	18.37
	Ni _{eq}	7.89	8.04	8.02	7.89	8.02	7.85	7.91	15.53	8.04
MELT5	Cr _{eq}	20.72	20.72	21.91	20.73	18.35	20.73	21.6	21.91	20.72
	Ni _{eq}	4.91	5.12	5.08	4.9	5.09	4.83	4.92	9.4	5.12
IC373	Cr _{eq}	30.35	30.35	32.73	31.3	25.59	31.08	31.78	32.89	30.35
	Ni _{eq}	5.89	10.33	10.21	7.45	9.87	7.27	9.57	12.08	10.33
IC378	Cr _{eq}	25.42	25.42	27.53	26.14	23.16	26.00	26.59	29.2	25.42
	Ni _{eq}	6.97	11.2	10.74	8.36	10.91	8.27	8.68	12.99	11.2
IC381	Cr _{eq}	26.00	26.00	28.52	26.85	23.73	26.71	27.21	30.82	26.00
	Ni _{eq}	7.51	11.77	11/16	8.92	11.59	8.94	9.03	13.6	11.77

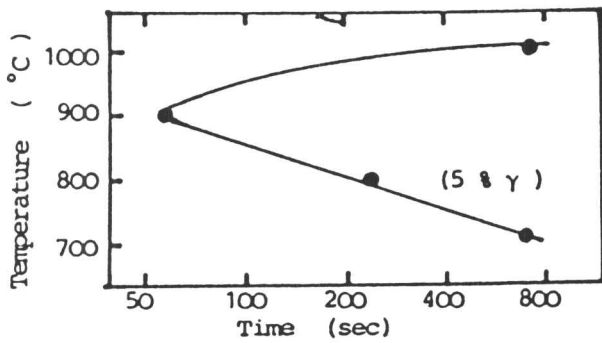
2.5 δ to γ Isothermal and Continuous Cooling Transformation Diagrams

2.5.1 Isothermal transformation diagrams

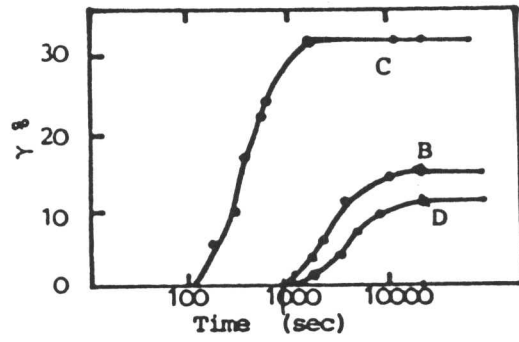
The isothermal transformation of δ -ferrite in Fe-0.08C-27Cr-5Ni-1.5 Mo wt.% duplex stainless steel has been described using a time-temperature transformation (TTT) diagram (Fig. 2.21) by Kuo (1955) [52]. He considered the diagram inaccurate and approximate because complete suppression of austenite precipitation was not achieved even with drastic quenching to the isothermal transformation temperature. The transformation diagram resembles that of the austenite to ferrite reaction in low-alloy steels in two respects: firstly, there is a single C-curve for the allotriomorphic transformation product, and secondly, the C-curve for the " δ eutectoid" product joins that for the low temperature acicular transformation product at about 800°C in such a way that they appear to form a continuous C-curve. After long holding times, FeCr sigma phase formation appears and that reaction also has its own C-curve.

Using optical microscopy and image analysis techniques Southwick [38] presented two TTT diagrams for a (Fe-0.03C-25Cr-5Ni-1.5Mo wt.%) duplex stainless steel. One was for specimens directly brought down from the ferritising temperature (T_δ) to the required isotherm and the other for the quenched specimens in which the high temperature ferrite was retained, and which were subsequently aged at the isothermal transformation temperature. A significant difference between the two curves is noticeable, Fig. 2.22. The "nose" of the reaction finish curve is pushed to higher temperature and shorter time for the quenched and aged specimens. This may be explained by the fact that the quenched specimens were not fully ferritic at room temperature and particles of austenite were already there in the matrix. In the present work it has been observed that even with the iced-brine quenched specimens, austenite particles are still observed in the matrix. Another possible explanation is that the introduction of quench strains, which provide defect structures on which nucleation can occur rapidly, might influence transformation kinetics.

Youzo [53], presented an isothermal transformation C-curve for quenched and aged (Fe-25Cr-5Ni-1.5Mo-0.11N wt.%) duplex stainless steel, Fig. 2.23. The effect of nitrogen in shifting the nose to a shorter time is clear when compared with the slower transformation observed for the directly reacted pure alloys (Fig. 2.23 a). The effect of the alloy composition on the maximum volume fraction of austenite at 900°C for the duplex stainless alloys listed in Table 2.4, is shown in Fig. 2.23 b.



a

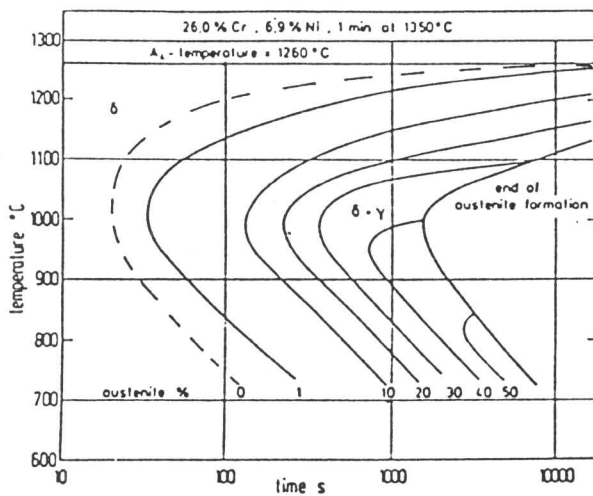


b

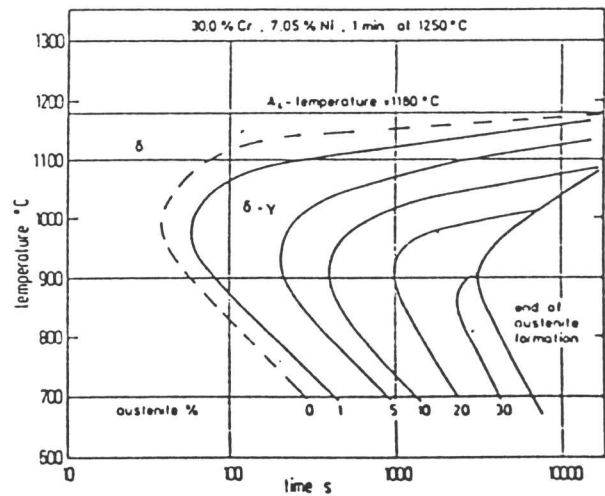
Fig. 2.23:

(a) TTT curve of γ in Fe-25Cr-5Ni-1.5Mo-0.11N wt.% duplex stainless steel.

(b) Isothermal transformation curves of γ at 900°C, compositions in Table 2.4 [53].



a



b

Fig. 2.24: TTT diagrams (a) Fe-26Cr-6.9Ni wt.% and (b) Fe-30Cr-7.05Ni wt.% [32].

Table 2.4: Composition of the alloys investigated by Youzo [53] in wt.%.

Alloy	Cr	Ni	Mo
B	25	5	1.5
C	25	6.7	1.5
D	24	3.8	—

As expected, the increase in nickel content has a remarkable effect on the maximum volume fraction of austenite, and the lower carbon and nitrogen contents slow down the δ to γ transformation. The incubation period for austenite formation is proportional to the Cr_{eq}/Ni_{eq} ratio and inversely proportional to the maximum volume fraction of γ . It is also longer in the directly transformed specimens than in the quenched and aged samples.

Isothermal transformation diagrams reported by Hoffmeister and Mundt [32,54] for two duplex stainless alloys are presented in Fig. 2.24; they show that increasing the Cr content and decreasing the Ni content lowers the ferritisation temperature, shifts the nose of the C-curve towards longer times and somewhat lower temperatures, and decreases the maximum volume fraction of austenite obtained at ambient temperature.

2.5.2 Discussion

On comparing the C-curves discussed earlier, it is clear that different results were reported by different workers. The reaction of δ to γ is sensitive to interstitials C and N. The presence of (0.08 wt.% C) in the alloy investigated by Kuo [52] led to an accelerated δ to γ reaction, with transformation beginning after just 2 seconds at 900°C. It also causes the formation of the “ δ eutectoid” termed reaction. The reaction in the (0.03 wt.% C) alloy investigated by Southwick [38] was shown to be somehow slower and the nose of the ‘C’ curve was placed at 725°C for the directly aged samples and at 900°C for the specimens aged from retained δ -ferrite after quenching to ambient temperature. The formation of “ δ eutectoid” was not represented. The reaction starts after 50 seconds at 900°C for the alloy investigated by Youzo *et al.* which contains 0.11 wt.% N, while a faster reaction start time was reported for pure alloys [32]. The disagreement between different C-curves could be a result of the effect of the interstitial additions which is not clearly understood, or to the fast δ to γ reaction which makes it difficult to obtain a fully ferritic structure at ambient temperature.

2.5.3 Continuous cooling diagrams

The only available continuous cooling transformation diagrams are those due to Mundt and Hoffmeister [54,32]. They were constructed using a hot stage light microscope. The continuous cooling transformation diagrams are shown in Fig. 2.25. As expected, they show that the transformation-start temperature for $\delta \rightarrow \gamma$ decreases with cooling rate and increases with an increase in nitrogen content.

2.6 Decomposition of δ in Duplex Stainless Steels

When duplex stainless steels are transformed isothermally, a wide variety of transformation products is obtained, consisting of mixtures of austenite, carbides, sigma phase and other phases in a complex range of morphologies and kinetic features.

During isothermal transformation at temperatures within the range of 1000-800°C, δ -ferrite ^{*} has been reported to transform into a “ δ eutectoid”. The implied reaction $\delta \rightarrow \gamma + \text{Cr}_{23}\text{C}_6$ does not seem to have been established to be a genuine eutectoid transformation, the term being used because of the morphological similarity between the $\gamma + \text{Cr}_{23}\text{C}_6$ mixture and conventional pearlite found in low-alloy steels. It is not even established that the γ and Cr_{23}C_6 phases grow co-operatively from δ [52,55-57]. Below 800°C the formation of an acicular aggregate of $\gamma + \text{Cr}_{23}\text{C}_6$ termed “ δ bainite” has been reported along the grain boundaries and in the interior of δ -ferrite grains. This terminology is however doubtful since there are no indications of an invariant plane strain (IPS) shape change accompanying transformation. The formation of austenite rods in Widmanstätten pattern has also been reported [57] along with sigma phase in the vicinity of 700°C. This is particularly the case with duplex stainless steel alloys containing between 0.08 and 0.24 wt.% carbon.

At low temperatures below 650°C, it appears that the austenite grows from the ferrite by a martensitic mechanism. In the same temperature range, chromium rich α' particles precipitates on $(001)_\alpha$ planes. The precipitates are small ($30 \times 6 \text{ \AA}$) and are coherent with the ferrite. They do not grow rapidly with time and eventually dissolve

^{*} Ferrite formed on solidification is known as δ -ferrite, while ferrite resulting from the transformation of austenite during cooling is termed α -ferrite.

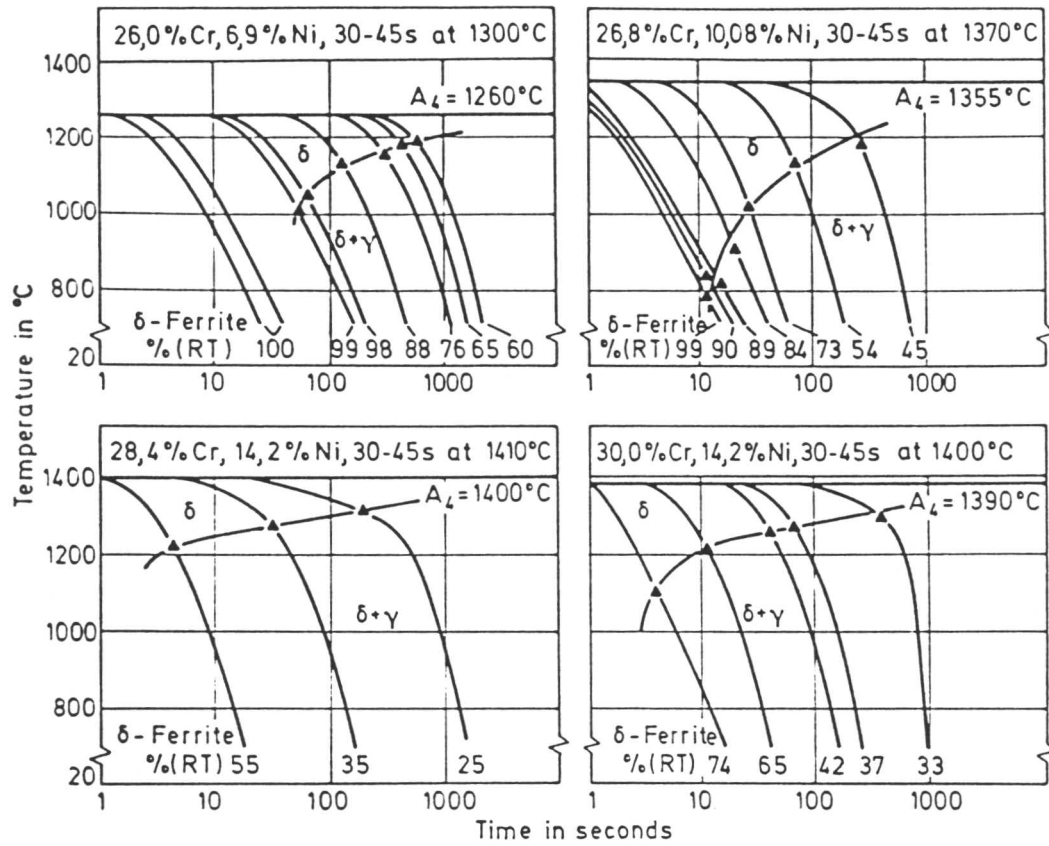


Fig. 2.25: Continuous cooling transformation diagrams for the start of $\delta \rightarrow \gamma$ transformation of duplex stainless steels with increasing chromium and nickel contents according to Mundt and Hoffmeister [54]. Chromium and nickel contents are stated for each diagram. Carbon, silicon and manganese contents are 0.02, 0.01 and 0.01-0.04 wt.% respectively (the term A_4 is the ferritisation temperature referred to as T_δ in the present work).

as the intragranularly nucleated austenite found at high temperatures is stimulated to form [38].

The decomposition of δ -ferrite under continuous cooling transformation conditions in (Fe-20Cr-10Ni wt.%) austenitic stainless steel has been reported for cooling rates between 20 to 15000°C s⁻¹ [58]. At a cooling rate of 20°C s⁻¹ allotriomorphic austenite grows on the primary δ boundaries and Widmanstätten austenite also forms. The retained δ is as a consequence enriched in Cr and depleted in Ni. In this respect, the Widmanstätten austenite is not a displacive reaction product like its counterpart the Widmanstätten ferrite in low-alloy steels. The retained δ -ferrite has a Kurdjumov-Sachs (K-S) type orientation relationship with austenite. At a cooling rate of $\approx 100^\circ\text{C s}^{-1}$, finer Widmanstätten austenite is formed. When the parent δ phase is coarse grained, and the cooling rate is higher the Widmanstätten austenite is replaced largely by allotriomorphic austenite. At still higher cooling rates, 7000 to 15000°C s⁻¹, the Widmanstätten transformation is completely suppressed and the microstructure consists of equiaxed austenite grains bounded by solute enriched rims ($\approx 100\text{ nm}$ wide) of retained δ . Unlike the δ associated with Widmanstätten austenite, those rims are not (K-S) related to the allotriomorphic austenite [58].

The transformation of deformed δ -ferrite during annealing has been investigated in (Fe-0.03C-0.7Si-0.7Mn-26Cr-5Ni-1.3Mo wt.%) duplex stainless steel [59]. Austenite particles precipitate extremely rapidly by heterogeneous nucleation on the dislocation networks characteristic of a deformed microstructure. The particles that form are of a rod shape at the early stages of annealing and adopt a more irregular shape at longer annealing times. Their orientation relationship with the ferrite is scattered about Nishiyama-Wasserman (N-W) and (K-S) orientation relationship during both nucleation and growth [43].

$$\begin{aligned} & \text{(N - W)} \\ & (\bar{1}10)_\alpha // (111)_\gamma \\ & [001]_\alpha // [\bar{1}01]_\gamma \end{aligned}$$

$$\begin{aligned} & \text{(K - S)} \\ & (110)_\alpha // (111)_\gamma \\ & [\bar{1}11]_\alpha // [\bar{1}10]_\gamma \end{aligned} \quad [43]$$

2.7 Sigma Phase Formation in Duplex Stainless Steels

σ is a hard and brittle intermetallic phase of nominal composition FeCr [60,61], although many other alloying elements are also soluble in its lattice. Its crystal structure consists of a tetragonal unit cell containing 30 atoms [62]. σ can form in many ferritic and austenitic stainless steels during prolonged ageing at temperatures between 500 and 950°C. Its formation adversely affects their mechanical properties, particularly impact strength [63], although its high hardness may be of use in hardfacing applications.

The precipitation of σ is rapid in duplex stainless steels, Fig. 2.26, because of their composition, the presence of δ -ferrite, and the role of δ/γ interfaces in helping the nucleation of σ , and because of the partitioning of alloying elements between δ and γ .

According to the literature, the role of the alloy chemistry on the isothermal transformation kinetics of the sigma phase is still not well defined. While Ellis and Pollard [64] observed sigma within a few minutes at 900°C in their studies on Fe-0.03C-0.07N-21Cr-7.4Ni-2.4Mo-1.3Cu wt.% duplex stainless steels. Beckitt [57] reported the formation of σ at a maximum rate at 700°C after one hour in duplex stainless steel of the composition (Fe-0.1C-25Cr-8Ni wt.%) Fig. 2.27. In the present work σ has been observed in the isothermally heated as welded duplex stainless steel weld metal after 15 minutes at 900°C at the primary δ grain boundaries. It may be the case that the higher carbon concentration in the alloy investigated by Beckitt [57] retarded the precipitation of σ by tying up the chromium and molybdenum to form chromium and molybdenum carbides.

Ferrite stabilisers are generally sigma promoters [65]. Mo and Si promote σ while Ni and C inhibit it [17]. Mn was also found to increase the rate and temperature of σ formation in duplex stainless steel castings, Fig. 2.28 [20]. It has been suggested that σ formation is always preceded by a cellular $M_{23}C_6 - \gamma$ structure, but it was also observed on a δ/γ boundary free of precipitation [38]. The following orientation relationships between austenite and σ phase are frequently observed:

$$\begin{aligned} (111)_\gamma // (001)_\sigma \\ [\bar{1}10]_\gamma // [\bar{1}10]_\sigma \end{aligned} \quad [19]$$

$$\begin{aligned} (111)_\gamma // (001)_\sigma \\ [0\bar{1}1]_\gamma // [140]_\sigma \end{aligned} \quad [66]$$

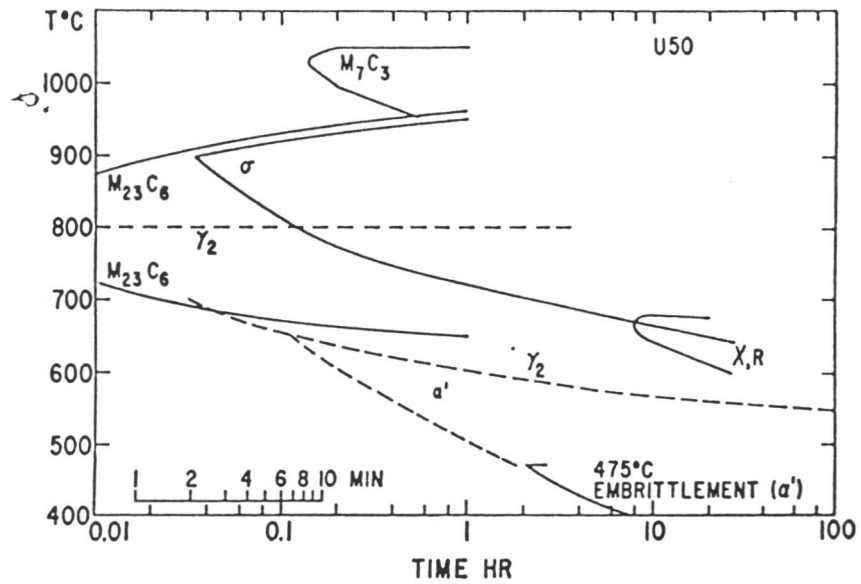


Fig. 2.26: TTP diagram for various phases observed in duplex stainless alloy Fe-0.03C-0.07N-21Cr-7.4Ni-2.4Mo-1.3Cu wt.% [68].

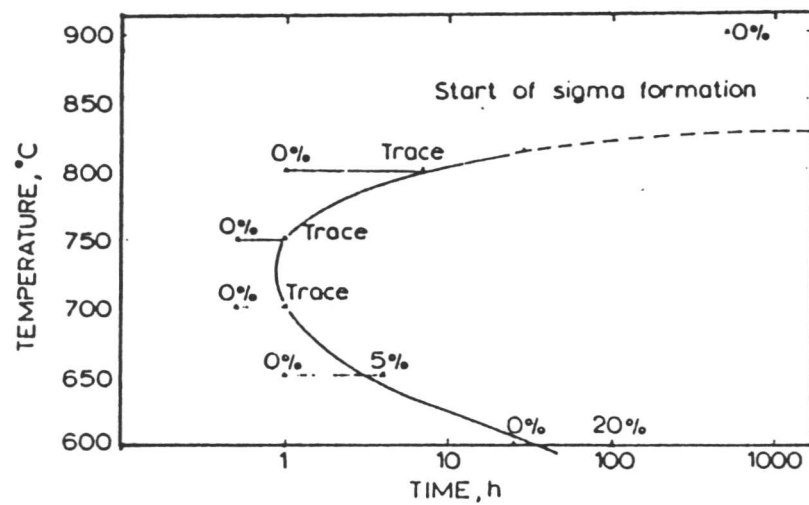


Fig. 2.27: C-curve showing rate of sigma formation in Fe-0.1C-25Cr-8Ni duplex alloy [57].

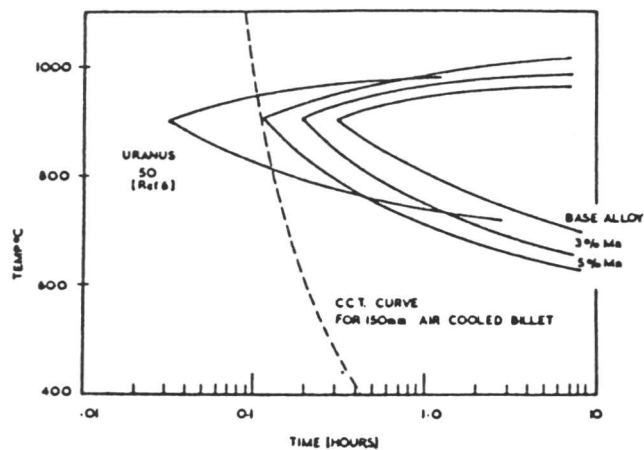


Fig. 2.28: Rate of formation of sigma phase in a series of duplex alloys containing manganese additions [39].

High levels of deformation accelerate σ formation [67]. σ was observed during the annealing of deformed δ -ferrite in duplex stainless steel after 3.6×10^3 s [59], but no clear evidence for the nucleation of σ on dislocations exists. It was actually suggested [69] that it is not the cold work itself that accelerates σ phase formation, but rather the recrystallisation that subsequently occurs during ageing, that acts as a catalyst in the σ phase formation process. It was also reported [70] that cold work alone without recrystallisation can hinder the σ phase transformation, suggesting that the moving recrystallisation front and the considerable atomic motion at this front are instrumental in promoting σ nucleation.

During superplastic deformation of duplex stainless steel (Fe-25Cr-6.5Ni-3Mo-0.14N wt.%) at 1173 K and 10^{-3}s^{-1} strain rate, σ phase was reported to precipitate dynamically by a eutectoid decomposition of δ -ferrite into γ and σ phases leading eventually to γ/σ equiaxed duplex structure after the dynamic recrystallisation of the soft austenite grains [71].

The mechanism by which sigma phase forms has been approached in many different ways. While Barick [72], who investigated austenitic stainless steels, believes that sigma phase formation is always preceded by carbide precipitation, Vitek and David [69] suggested that it is nucleation controlled; they concluded, from their investigation in wrought and welded stainless steels (Table 2.5), that the long range diffusion necessary to produce chromium rich sigma phase plays only a secondary role in the sigma phase transformation and is not rate controlling.

Table 2.5: Compositions (wt.%) of alloys used in the investigation reported in [69].

Alloy	Cond.♣	Cr	Ni	Mn	Si	C	S	N	P	Ti	B
308	H	20.9	10.3	1.6	0.49	0.068	0.012	0.039	0.018	<0.01	<0.001
308	W	20.2	9.4	1.8	0.46	0.053	0.008	0.058	0.018	<0.01	0.002
308CRE	H	20.0	10.0	2.0	0.62	0.043	0.015	0.011	0.011	0.57	0.002
308CRE	W	19.8	9.9	2.0	0.61	0.036	0.014	0.022	0.022	0.50	0.003

♣ Cond. = condition, H = homogenized and W = welded.

It has been suggested recently [73] that the crystallographic characterisation and the morphology of the δ -ferrite plays an important role in the formation of σ phase at elevated temperatures in austenitic stainless steel weld metal 304L (Table 2.6). While

of hydrogen in ferrite and martensite is much lower than in austenite at room temperature. In the case of austenitic stainless steel weld metals, lower diffusivity and higher solubility of hydrogen in the austenite reduces the susceptibility to cracking but often leads to the formation of porosity [74].

Duplex stainless steels are believed to be embrittled by hydrogen. Hydrogen was found to have the effect of reducing the ductility of duplex stainless steels Fe-25Cr-7Ni-3.3Mo-0.9Mn-0.3W-0.14N-0.02C and Fe-22Cr-5Ni-3.0Mo-1.6Mn-0.14N-0.02C wt.% when they were charged cathodically, thermally or in a N. A. C. E. solution and irrespective of whether the specimens were strained simultaneous to, before or after the charging. Cathodic charging is believed to be effective in crack initiation since the hydrogen evolved is diffusive and usually concentrated at the surfaces, while thermal hydrogen, which is usually found trapped and distributed throughout the specimen cross section, becomes mobile on the onset of necking which is in turn believed to enhance the crack growth. Hydrogen embrittlement in duplex stainless steels is also thought to be assisted by dynamic straining, particularly at low strain rates and with coarse δ -ferrite grain size microstructures. The negative role of the large δ grains is believed to be a consequence of the deformation mechanism occurring by macrotwinning rather than slip. Based on this, it was suggested that a microstructure consisting of a large volume fraction (about 0.5) of equiaxed small particles of austenite in a ferrite matrix would have a better resistance to hydrogen embrittlement if it is heat treated such that deformation occurs by slip rather than macrotwinning [75].

19. Mundt, R. and Hoffmeister, H. (1983) Arch. Eisenhüttenwes, **54** (6), p. 253.
20. Gordon, G. M., in Proc. Firming Conf. NACE, Houston, Texas (1977), p. 893.
21. Abron, R. H. and Bain, E. C. (1930) Trans. Amer. Soc. Steel Treating, **8**, p. 837.
22. Farrar, R. A. (1987) J. Mat. Sci., **22**, p. 363.
23. Cox, J. B. and Eckel, J. T. (1969) J. Mat. Sci., **4**, p. 282.
24. Colombier, L. and Hoffman, J. (1967) 'Stainless and Heat Resisting Steels', Edward Arnold.
25. Metals Handbook (1973), 8th edition, Vol. **8**, American Society for Metals.
26. Hoffmeister, H. and Mundt, R. (1981) Arch. Eisenhüttenwes., **52** (4), p. 159.
27. Pickering, F. B., Conf. Proc. Stainless Steels '84, Göteborg, Sept. 1984, The Inst. of Metals, London (1985), p. 2.
28. Folkhard, E. 'Welding Metallurgy of Stainless Steels' (1988) Wien-New York, Springer-Verlag publishers, p. 25.
29. Bechtoldt, C. J. and Vacher, H. C. (1957) J. Res. Nat. Bur. Stand., **58**, p. 7.
30. Folkhard, E. 'Welding Metallurgy of Stainless Steels' (1988) Wien-New York, Springer-Verlag publishers, p. 36.
31. Sump, C. H. and Bodine, G. C. (1983) 'Duplex Stainless Steel', ed. R. A. Lula, Publ. by American Society for Metals, p. 71.
32. Mundt R. and Hoffmeister, H., Conf. Proc. Stainless Steels '84, Göteborg, sept. 1984, The Inst. of Metals, London (1985), p. 315.
33. Schuller, H. J. (1965) Arch. Eisenhüttenwes, **34**, p. 61.
34. Kubaschewski, O. 'Iron-Binary Phase Diagrams' (1982) Berlin-Heidelberg-New York, Springer; Dusseldorf, Verlag Stahleisen m. b. H.
35. Horn, E. M. and Kugler, A. (1977) Werkst.-Techn., **8**, p. 362.
36. Masumoto, I. and Imai, Y. (1964) Sci. Rep. Res. Ins. Tohoku Univ., Nagoya, Ser. A., p. 16.
37. Ohmori, Y. and Maehara, Y. (1984) Trans. ISIJ, vol. **24**, p. 60.
38. Southwick, P. D. (1978) Ph.D. Thesis, University of Cambridge, Dept. of Mat. Sci. and Metallurgy.
39. Chance, J., Coop, W. and Gradwell, K. J. (1983) 'Duplex Stainless Steels', ed. R. A. Lula, Publ. by American Society for Metals, p. 371.

40. Easterling, K. 'Introduction to the Physical Metallurgy of Welding' publ. by Butterworths, London (1983).
41. Folkhard, E. 'Welding Metallurgy of Stainless Steels' (1988) Wien-New York, Springer-Verlag publishers, p. 42.
42. Solyu, B. Ph.D. Thesis (1988) Cambridge University, Dept of Mat. Sci. and Metallurgy.
43. McKenzie, S., Flower, H. M. and West, D. R. F., Conf. Proc. Stainless Steels '84, Gsteborg, Sept. 1984, The Inst. of Metals, London (1985), p. 77.
44. Schaeffler, L. A. (1949) Metal Progress, **56**, p. 680.
45. Seferian, D. (1959) Metallurgie de la Soudure, Dunod, Paris.
46. Skuin, K. and Kreyssing, T. (1978) Neue Hutte, **23** (1), p. 22.
47. Honeycombe, J. and Gooch, T. G. (1985) The Weld. Inst. Report 286/ 1985.
49. Suutala, N., Takalo, T. and Mosio, T. (1979) Met. Trans., **10A**, p. 513.
50. Noble, D. N. and Gooch, T. G. (1986) The Weld. Inst. Report 321/1986.
51. Maehara, Y. et al. (1983) Metal Science, **17**, p. 541.
52. Kuo, K., (1955) JISI, **181**, p. 134.
53. Yuzo, H., Hiroshi, O. and Noboru, W. (1984) Trans. ISIJ, **24**, p. 398.
54. Mundt, R. and Hoffmeister, H. (1983) Arch Eisenhüttenwes, **54** (8), p. 333.
55. Nehrenberg, A. E. and Lillys, P. (1954) Trans. ASM, **46**, p. 1176.
56. Castro, R. J. and Tricot, R. (1962) Rev. Met., **9**, LIX.
57. Beckitt, F. R. (1969), JISI, **207**, p. 632.
58. Singh, J., Purdy, G. R. and Weatherly, G. C. (1985) Met. Trans., **16A**, p. 1363.
59. Parayil, T. R. and Howell, P. R. (1986) Mat. Sci. and Tech., **2** (11), p. 1131.
60. Lai, J. K. L. (1983) Mat. Sci. and Eng., **58**, p. 195.
61. Lai, J. K. L., Chastell, D. J. and Flewitt, P. E. J. (1981) Mat. Sci. and Eng., **49**, p. 19.
62. Weiss, B. and Stickler, R. (1972) Met. Trans., **3**, p. 851.
63. Langeborg, R. (1967) Trans. ASM, **60**, p. 67.
64. Ellis, R. G. and Pollard, G. (1970) JISI, p. 783.
65. Honeyman, G. A. and Towers, T. A. (1984) Mat. Res. Soc. Symp. Proc.

66. Lewis, M. H. (1966) *Acta Met.*, **14**, p. 1421.
67. Maehara, Y. et al. (1983) *Trans. ISIJ*, **23**, p. 247.
68. Solomon, D. and Devine, T. M., Conf. Proc., 'Duplex Stainless Steels', St. Louis, USA (1982) Publ. by ASM (1983), p. 693.
69. Vitek, J. M. and David, S. A. (1986) *Weld. J., Res. Suppl.*, Vol. **65**, No. 4, p. 106s.
70. Singhal, L. K. and Martin, J. W. (1968) *Acta Met.*, **16**, p. 1441.
71. Maeahra, Y. and Ohmori, Y. (1987) *Met. Trans. A*, **18A**, p. 663.
72. Barick, J. (1988) *Mat. Sci. and Tech.*, vol., **4**, p. 5.
73. KoKawa, H., Kuwana, T. and Yamamoto, A. (1989) *Weld. Res. Suppl.*, Vol. **68**, No. 3, p. 92s.
74. Folkhard, E. 'Welding Metallurgy of Stainless Steels' (1988) Wien-New York, Springer-Verlag publishers, p. 48.
75. Cohen, L., (1988) Ph.D. Thesis, University of Cambridge, Dept. of Mat. Sci. and Metallurgy.
76. Fisher, R. M. et al. (1953) *Trans. AIME*, **197**, p. 690.
77. Williams, R. O. (1974) *Met. Trans.*, **5**, p. 967.
78. Chandra, D. and Schwartz L.H. (1971) *Trans. AIME*, **12**, p. 511.

Chapter 3

METALLURGY OF DUPLEX STAINLESS STEEL WELDS

3.1 Introduction

Unlike casting, weld metal microstructures cannot usually be modified by hot forming and post-welding heat treatment procedures, and hence lack the processing ability by which harmful precipitation and segregation effects are controlled in the base plates. Weld metal properties are influenced largely by the metallurgical reactions that take place during solidification and subsequent cooling of the solidified weld metal and it is often the case that the user is stuck with that final microstructure.

Adjusting the chemistry of the welding pool is a technique often applied to produce a weld metal with matching microstructure to that of the base plate. This technique, although beneficial in the weld zone, does not solve by any means the problems in the as-welded and the heat affected zones (HAZ). The use of rapid cooling solidification in any attempt to produce fine grained weld metals or to avoid harmful precipitation by supercooling, would be disastrous for duplex stainless steels by suppressing the δ -ferrite to austenite solid state transformation.

Duplex stainless steels, apart from some near ferritic alloys with a low alloy content, do not undergo a secondary transformation from austenite to ferrite as is usually experienced by low-alloy and carbon steel weld metals.

3.2 Solidification

3.2.1 Primary crystallisation of the weld pool

A major characteristic of all welds produced by fusion welding processes is the continuous melting and subsequent solidification of a relatively small volume of the metal [1]. According to Savage *et al.* [2], heterogeneous nucleation of the solid phase from the liquid phase by inclusions is of a minor importance in fusion welding compared with crystal growth, because the crystals which precipitate from the liquid weld metal can grow directly from a solid base plate, *i.e.* epitaxially. Unlike the solidification of ingots, the crystallisation process in welding is almost completely controlled by the dissipation of heat into the solid base plate, with only a small amount of heat being dissipated into the surrounding atmosphere. This usually has a decisive influence on the type, size, anisotropy and crystallographic orientation of the crystals [3].

3.2.2 Microsegregation

During the solidification of alloys, the precipitate crystals generally have a different composition relative to the average alloy composition (Fig. 3.1). If the cooling rate during solidification is high, then a state of nonequilibrium is created, and after solidification the system tries to return to equilibrium by way of diffusion.

During welding there is insufficient time for the solid phase to readjust continuously to the changing equilibrium conditions, so that a cored solid consisting of layers of different chemical compositions is obtained. This process is called microsegregation. The composition difference between the core of the crystal and its outer layer will increase with: increasing difference of composition between the liquidus and the solidus curves of the phase diagram, with decreasing slopes of these phase boundaries, with decreasing solute diffusion rate coefficients, and with diminishing time span available for homogenisation by diffusion during cooling (cooling rate) [4].

Compared with the state of equilibrium, the process of solidification is generally accompanied by a drop in solidus temperatures, and there is also an increase in segregation with the composition of new layers being shifted during crystal growth towards the dotted line from 1' to 4 (Fig. 3.2 a). Due to the impeded equalisation of concentration, their composition can only approach to a limited extent that of alloy L by way of diffusion. At the end of solidification the enriched melt with a composition 4'' will solidify as a thin film on the grain boundaries between the crystals. In the case of a multinary mixture with a eutectic point, a eutectic E will be precipitated in alloy D, (Fig. 3.2 b). Rapid cooling rates intensify microsegregation by a more severely impeded equalisation of concentration [4].

The segregation phenomena at the liquid/solid interface based on the impeded equalisation approach as represented by Folkhard [5], is shown in Fig. 3.3. To simulate the reality of the weld pool, it was assumed that the homogenisation is impeded more in the precipitated solid than in the melt, because it is believed that strong agitation occurs in the weld pool leading to mixing in the liquid ahead of the solid/liquid interface.

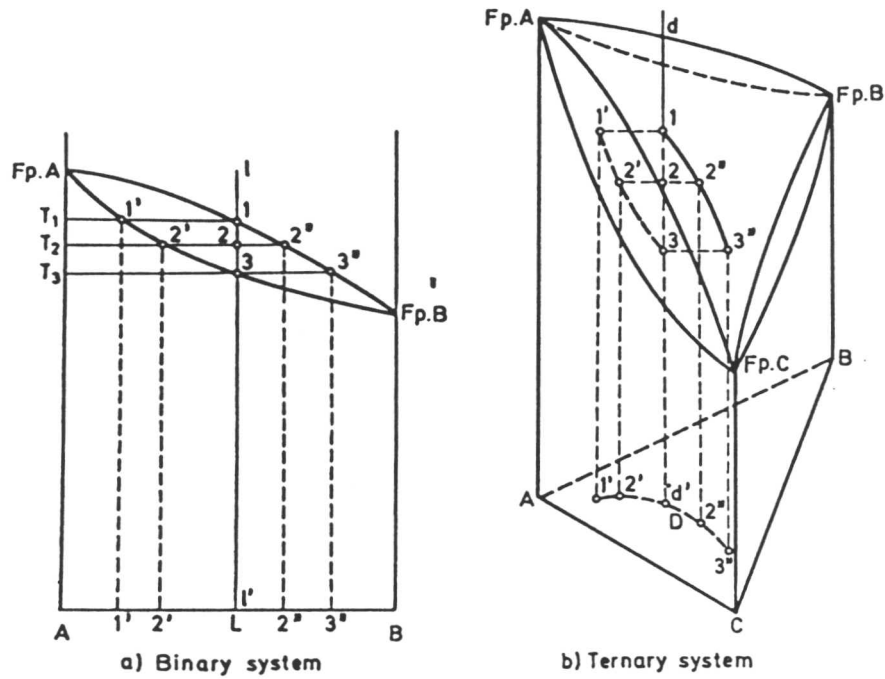


Fig. 3.1: The process of solidification in binary and ternary systems. The temperature is plotted on the vertical axis, with composition on each of the horizontal axes [6].

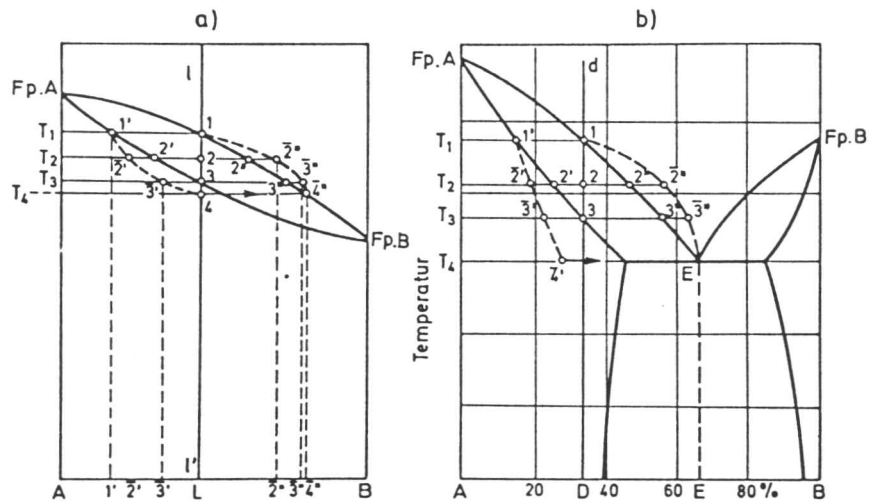


Fig. 3.2: Course of solidification in the state of nonequilibrium. Segregation due to impeded equalisation of concentration [4].

(a) binary mixture with complete solubility.

(b) quasi-binary profile of a ternary system with a eutectic E.

In both *a* & *b* The temperature is plotted on the vertical axis and the composition on the horizontal axis [4].

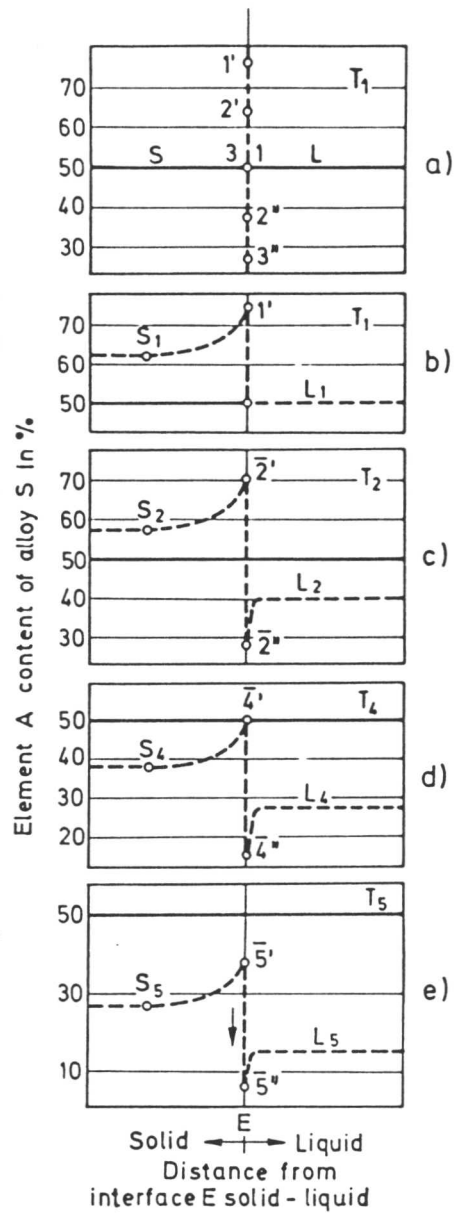


Fig. 3.3: Formation of liquid-solid interface during solidification (schematic). (a) full equalisation of concentration (ideal state), (b) – (e) impeded equalisation of concentration (real state), (b) start of solidification at temperature T_1 , (c) & (d) during solidification at temperatures T_2 and T_4 respectively, (e) state at the end of solidification at temperature T_5 [5].

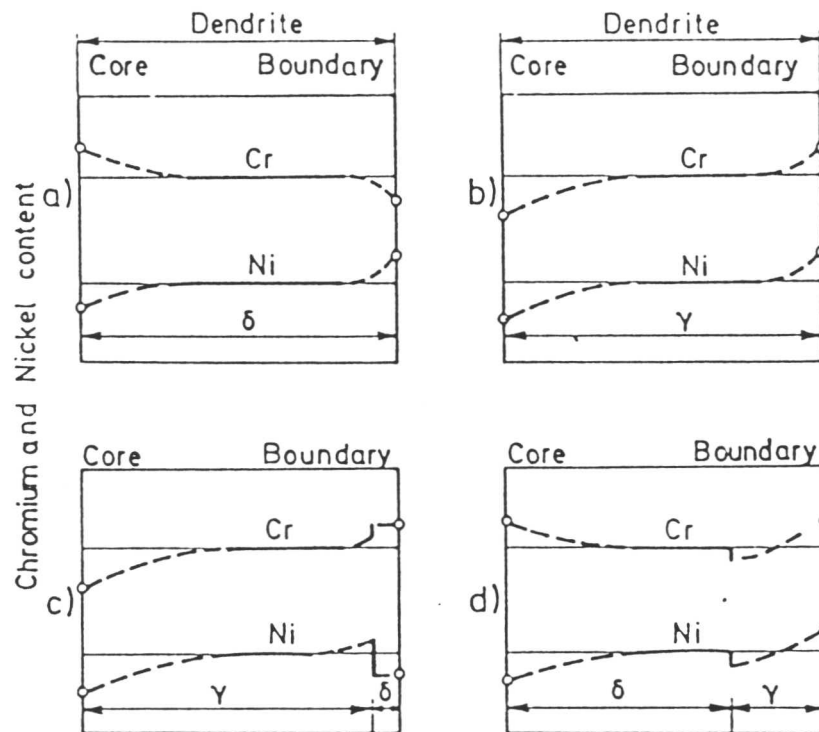


Fig. 3.4: Schematic representation of segregation and the distribution of chromium and nickel within dendrites during solidification of austenitic weld metals alloy [10]. (a) Complete solidification to δ -ferrite, (b) complete solidification to austenite, (c) partial solidification to austenite with precipitation of δ in the area of the residual melt, (d) formation of δ at the beginning of solidification and of austenite from the residual melt at the end of solidification.

Diffusion coefficient in cm ² /s										
Element	$\alpha(\delta)$ -Iron					γ -Iron				
	Temperature °C					Temperature °C				
	20	400	800	1100	1400	20	400	800	1100	1400
$\alpha(\gamma)$ -Fe	10 ⁻⁴⁶	10 ⁻¹⁹	10 ⁻¹²	10 ⁻⁹	10 ⁻⁷	10 ⁻⁵³	10 ⁻²²	10 ⁻¹⁴	10 ⁻¹¹	10 ⁻⁹
Al			10 ⁻¹¹	10 ⁻⁹	10 ⁻⁷	10 ⁻³⁶	10 ⁻¹⁵	10 ⁻⁹	10 ⁻⁸	
B						10 ⁻²⁰	10 ⁻⁹	10 ⁻⁶	10 ⁻⁵	
C	10 ⁻¹⁷	10 ⁻⁸	10 ⁻⁵	10 ⁻⁴		10 ⁻²⁷	10 ⁻¹³	10 ⁻⁸	10 ⁻⁶	
Cr	10 ⁻⁴²	10 ⁻¹⁸	10 ⁻¹¹	10 ⁻⁹	10 ⁻⁷	10 ⁻³⁷	10 ⁻¹⁸	10 ⁻¹³	10 ⁻¹¹	10 ⁻⁹
Co	10 ⁻⁴⁴	10 ⁻¹⁹	10 ⁻¹²	10 ⁻¹⁰		10 ⁻⁶⁸	10 ⁻²⁶	10 ⁻¹⁶	10 ⁻¹²	
Cu			10 ⁻¹¹	10 ⁻⁹		10 ⁻⁴⁹	10 ⁻²⁰	10 ⁻¹²	10 ⁻¹⁰	
H	10 ⁻⁵	10 ⁻³	10 ⁻³	10 ⁻³		10 ⁻¹⁰	10 ⁻⁵	10 ⁻⁴	10 ⁻³	
Mn						10 ⁻⁵³	10 ⁻²²	10 ⁻¹⁴	10 ⁻¹¹	10 ⁻⁹
Mo	10 ⁻⁴⁶	10 ⁻¹⁸	10 ⁻¹¹	10 ⁻⁹	10 ⁻⁷	10 ⁻⁴⁹	10 ⁻²¹	10 ⁻¹³	10 ⁻¹¹	10 ⁻⁹
N	10 ⁻¹⁷	10 ⁻⁸	10 ⁻⁶	10 ⁻⁵		10 ⁻³¹	10 ⁻¹³	10 ⁻⁸	10 ⁻⁷	
Nb								10 ⁻¹³	10 ⁻¹¹	10 ⁻⁹
Ni	10 ⁻⁴⁵	10 ⁻¹⁸	10 ⁻¹¹	10 ⁻⁹		10 ⁻⁵⁴	10 ⁻²³	10 ⁻¹⁵	10 ⁻¹¹	10 ⁻⁹
P	10 ⁻³⁴	10 ⁻¹²	10 ⁻⁸	10 ⁻⁷	10 ⁻⁶			10 ⁻¹⁴	10 ⁻⁹	10 ⁻⁸
S			10 ⁻¹⁰	10 ⁻⁸	10 ⁻⁶	10 ⁻³⁹	10 ⁻¹⁶	10 ⁻¹⁰	10 ⁻⁹	10 ⁻⁷
Si	10 ⁻⁵⁰	10 ⁻²¹	10 ⁻¹³	10 ⁻¹¹	10 ⁻⁷	10 ⁻⁴⁸	10 ⁻²⁰	10 ⁻¹³	10 ⁻¹²	10 ⁻⁹
Ti	10 ⁻⁴⁷	10 ⁻¹⁹	10 ⁻¹²	10 ⁻⁹	10 ⁻⁷	10 ⁻⁴⁹	10 ⁻²¹	10 ⁻¹³	10 ⁻¹¹	10 ⁻⁹
V			10 ⁻¹²	10 ⁻⁹	10 ⁻⁷			10 ⁻¹⁴	10 ⁻¹¹	10 ⁻⁹
W	10 ⁻⁶⁰	10 ⁻²⁶	10 ⁻¹⁷	10 ⁻¹⁰		10 ⁻⁶⁸	10 ⁻³⁰	10 ⁻²⁰	10 ⁻¹⁶	

Table 3.1: Survey of diffusion constants of alloying elements in α (δ) and γ iron, including the values for self diffusion of iron. Most of the data at 20°, 400°, 800° and 1100°C are calculated values [17]. They were supplemented by data from the review by Fridberg *et al.*, [18,19]

3.2.3 Crystal Growth During Solidification

According to Tiller [20], the crystal interface configuration depends on the differences occurring between the local liquidus temperatures and the respective real temperatures of the melt, produced by external cooling parameters. Constitutional supercooling can occur and influence the stability of the interface.

The effect of cooling rate and direction of base material crystallisation on crystal configuration, crystal direction and constitutional supercooling, according to Savage [21], is shown in (Fig. 3.5). High cooling rates tend to promote a cellular solidification mode, while medium cooling rates lead to dendritic instabilities. In stainless steel weld metals the solidification mode is generally cellular-dendritic. The direction of growth is determined strongly by the direction of greatest dissipation of heat [22]. A theoretical model for the constitutional supercooling at the liquid/solid interface at the surface of the weld pool as suggested by Wittke [23] is shown in Fig. 3.6. The highest values of supercooling are located at the bead centerline.

3.2.4 Primary Crystallisation of Stainless Steel Welds

Stainless steel weld metals can solidify from the liquid state to either primary δ -ferrite or to primary austenite crystals depending on the chemical composition of the alloy. If an alloy happens to fall in the ternary constitution diagram in the area of the eutectic groove and passes through the three phase triangle ($L+\gamma+\delta$) during solidification, a mixture of primary δ -ferrite and austenite may be formed. Primary solidified δ -ferrite alloys can subsequently undergo a solid state transformation from δ -ferrite to austenite and/or austenite to ferrite during further cooling.

A model for weld metal solidification in austenitic and duplex stainless steels based on the chromium equivalent/nickel equivalent ratio Cr_{eq}/Ni_{eq} of the Schaeffler diagram, was proposed by Suutala *et al.*, [24-26] Fig. 3.7. In their model they classified five possible types of solidification: Type A, for a Cr_{eq}/Ni_{eq} ratio <1.3 when the weld metal solidifies completely to γ and no further high temperature transformation takes place. Type B, for a Cr_{eq}/Ni_{eq} ratio <1.48 , when γ is found to be the leading phase during solidification and δ solidifies from the rest of the melt between the cells or

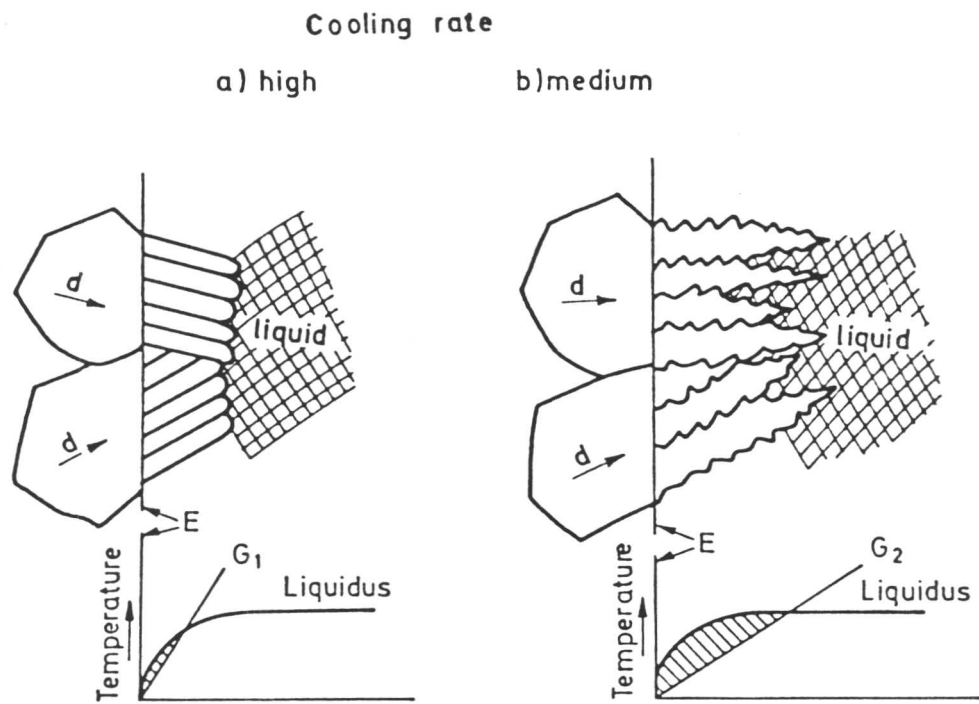


Fig. 3.5: Crystal configurations of weld metal at differing constitutional supercooling at the liquid-solid interface “E” caused by different temperature gradients G_1 and G_2 at varying cooling rates [21]. d = direction of crystallisation of base material crystals.

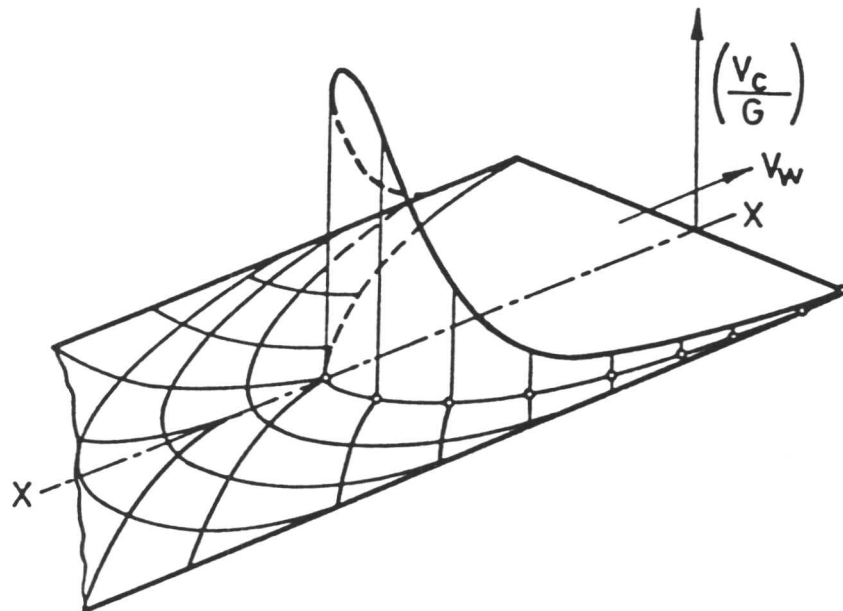


Fig. 3.6: Distribution of crystallisation parameter “constitutional supercooling” at the liquid-solid interface of a weld pool [23].

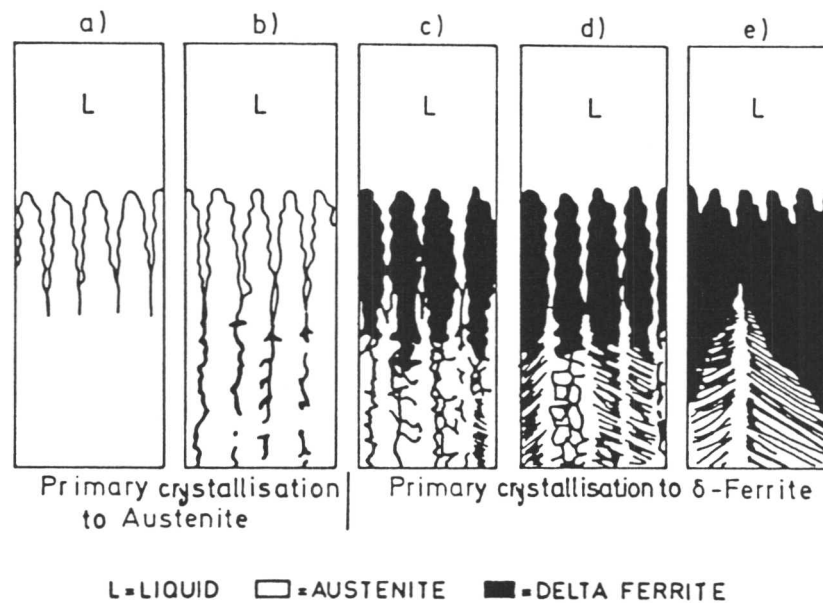


Fig. 3.7: Proposed solidification model for austenitic and austenitic-ferritic weld metals (schematic): (a) Type A, the weld metal solidifies completely to austenite and no further high temperature transformation takes place. (b) Type B austenite is the leading phase and δ -ferrite solidifies from the rest of the melt. (c) Type C, δ -ferrite is the leading phase, austenite solidifies from the rest of the melt and a quick phase transformation $\delta \rightarrow \gamma$ takes place at high temperatures. (d) Type D, as (c), but a higher volume fraction of ferrite is present at room temperature. (e) Type E, The weld metal solidifies completely to δ -ferrite and austenite forms through a solid state transformation [24].

dendrites so that the solidification takes a eutectic character. Types C & D, for Cr_{eq}/Ni_{eq} ratio less than 1.95 and more than 1.48, when δ is the leading phase and γ solidifies from the rest of the melt interdendritically by a peritectic reaction, or eutectically grows in the δ as the temperature decreases. In type C, a quick δ -ferrite to austenite phase transformation takes place at high temperatures resulting in a higher volume fraction of austenite at ambient temperature. In type D, the volume fraction of δ -ferrite is higher than that of type C. With mode type E, for Cr_{eq}/Ni_{eq} ratio >1.95 , the weld metal solidifies as δ completely and γ forms through a solid state transformation.

Valtierra *et al.*, [27] studied the effect of nitrogen additions to the argon shielding gas on autogenously (*i.e.* without a filler metal) welded duplex stainless steel using the tungsten inert gas technique. They reported a change of the solidification mode within the same weld bead from type D mentioned earlier to type E. In agreement with Suutala *et al.* they observed that the change from type E to a mixture of E and D types occurs at a Cr_{eq}/Ni_{eq} ratio of ≈ 2.3 and the change from type D to a mixture of types D and E occurs at Cr_{eq}/Ni_{eq} ratio of ≈ 2.1 . They suggested Cr_{eq}/Ni_{eq} ratios different from those of Suutala *et al.* as a different coefficient for the contribution of nitrogen was used.

In arc welded (Fe-22Cr-6Ni-3Mo-0.14N wt.%) duplex stainless steel, matching composition weld metal solidifies to δ with epitaxial growth from the heat affected zone giving a coarse structure [28]. This problem is usually associated with epitaxial growth in high energy processes such as submerged arc and electroslag welding, where the initial crystal size inherited from the grain growth area of the base plate can be rather large [29].

3.2.5 Cooling Rate

In principle, the cooling rate of weld metals, for arc welds, is determined on the one hand by the amount of heat supplied per unit length (heat input) and on the other hand by the rate of heat flow which occurs predominantly through the base metal surrounding the bead. The cooling rate affects both constitutional and thermal supercooling of the weld pool. Investigations on the cooling phenomena in the heat affected zone during electric arc welding of stainless steel suggest that the time for solidification is just as short in stainless steel as that of low alloy-steels [30, 31, 32]. According to Zitter [30], the thermal conductivities of stainless steels and low-alloy steels are equal at 1200°C being approximately $33 \text{ J cm}^{-1} \text{ s}^{-1} \text{ }^\circ\text{C}$.

The crystal growth rate of some weld metals in GTAW spot welds was found to be in the range 2 to 8 mm s⁻¹, with these values being influenced primarily by the cooling rate of the weld pool [33], which supports the assumption that both supercooling and impeded equalisation of concentration must occur during the solidification of weld metal in electric arc welding of stainless steel. This is also in agreement with the conclusion drawn by Lippold and Savage [34] who have assumed that the readjustment of concentration through diffusion on the solid side of the liquid/solid interface will be rather limited in the case of solidification of austenitic stainless steel weld metal.

At a cooling rate of 0.1°C s⁻¹, thermal supercooling of the liquidus and solidus temperatures of about 30-60 and 80-120°C respectively were reported for Cr-Ni alloys with compositions ranging from 20 to 26 wt.% Cr and 10 to 21 wt.% Ni. Higher supercoolings are expected in electric arc welding since cooling rate is much higher than 0.1°C s⁻¹. Far higher supercoolings are obtained in electron beam welding [35], although the degree of supercooling is limited by the fact that the solidification process involves simply the propagation of base metal grains into the liquid metal [36].

3.3 $\delta \rightarrow \gamma$ Transformation in Stainless Steel Weld Metals

During electric arc welding, the process of $\delta \rightarrow \gamma$ transformation occurs over a very short period of time, typically one to two seconds. The new formation of austenite starts at the grain boundaries of the δ -ferrite crystals which are believed to be nickel enriched and chromium depleted due to segregation during solidification; these areas provide an ideal nucleation site for austenite. In (Fe-20Cr-10Ni wt.%) stainless steel weld metal, the reported composition of the residual ferrite is in the range 23-26 wt.% Cr and 5-8 wt.% Ni. Although it does not seem easy by any means to distinguish between the segregation during solidification from that of partitioning due to δ to γ transformation [37], it is suggested [38] that there is always an overlap of these two processes, with the δ to γ transformation accounting for the bigger share.

The morphology of the residual ferrite in stainless steel weld is determined by the primary solidification mode and the subsequent δ to γ solid state transformation. A skeleton like morphology is produced with primary solidification to austenite, while vermicular and lathy morphologies are obtained with primary solidification to ferrite. With increasing Cr_{eq}/Ni_{eq} ratios, as in duplex stainless steels, the δ to γ transformation will start at progressively lower temperatures, allowing the recrystallised ferrite to grow coarser and resulting in a higher volume fraction of ferrite at ambient temperature [39].

In stainless steel weld metals that solidify completely to δ there is general agreement on the importance of cooling rate on the δ to γ transformation. In GTA weld deposits, increasing welding speed was associated with higher volume fractions of δ at ambient temperature [12].

3.4 Duplex Stainless Steel Weld Metals

3.4.1 Weld microstructure

Most duplex stainless steel weld metals solidify completely to δ -ferrite according to the solidification mode E (Suutala *et al.* [24]), discussed in the previous section, because their Cr_{eq}/Ni_{eq} ratio is in general more than 1.9. The volume fraction of austenite is determined by subsequent solid state phase transformation.

The δ to γ transformation is primarily a function of material composition and thermal cycle. In fusion welding the metal is intensively heated to raise its temperature to the melting point. The peak temperature achieved in the heat affected zone is more than the ferritisation temperature (T_δ) and a complete transformation to δ , with concomitant grain coarsening takes place. On cooling, reformation of austenite at the δ grain boundaries and within the δ grains occurs. Weld metals with matching composition solidify epitaxially with respect to δ in the heat affected zone, giving a coarse columnar structure. A similar transformation to that of the HAZ takes place during cooling [28,40]. A typical weld microstructure consists of elongated δ grains, intergranular networks of Widmanstätten austenite and fine intragranular acicular γ , Fig. 3.8. Reheated zones between passes of the weld generally have a higher volume fraction of γ as a result of further transformation of δ from the δ and γ region to γ [41].

Weld microstructure can be sensitive to alloy composition. Duplex stainless steel weld metals of the compositions, Fe-29Cr-9Ni wt.%, Fe-25Cr-5Ni-1.5Mo wt.% and Fe-22Cr-9Ni-3Mo-N wt.% (with Cr_{eq}/Ni_{eq} ratios of 2.15, 4.1 and 2.4 respectively), all



Fig. 3.8: Typical microstructure of duplex stainless steel weld metal, δ -ferrite (*dark*), austenite (*light*).